

RICE UNIVERSITY

***In-vitro* Model System for Calcific Band Keratopathy  
and Inhibitory Effects of C<sub>60</sub> Fullerene Derivatives**

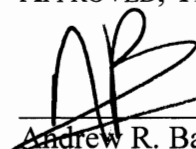
by

**Nadjmeh Doostdar**

A THESIS SUBMITTED  
IN PARTIAL FULFILLMENT OF THE  
REQUIREMENTS FOR THE DEGREE

**Doctor of Philosophy**

APPROVED, THESIS COMMITTEE:



Andrew R. Barron, Chair  
Charles W. Duncan, Jr. – Welch Chair of  
Chemistry and Professor of Materials Science



Lon J. Wilson  
Professor of Chemistry



Mason Tomson  
Professor of Environmental Engineering



Marshal B. Hamill  
MD, Associate Professor, Department of  
Ophthalmology

HOUSTON, TEXAS  
AUGUST 2010

## Abstract

### *In-vitro* Model System for Calcific Band Keratopathy and Inhibitory Effects of C<sub>60</sub> Fullerene Derivatives

by

Nadjmeh Doostdar

Calcific band keratopathy (CBK) is a degenerative condition resulting in the deposition of calcium salts in the superficial layers of the cornea and causing significant visual disturbance and pain of the affected eye. The amount of CBK precipitates recovered from the affected eye is very small rendering a great challenge in development of an effective and non-invasive treatment for this condition. This provides an impetus to study the possible chemical factors that may contribute to the development of CBK in an effort to develop a more efficient and un-intrusive treatment for this condition. To this end, we have developed an *in-vitro* model system resembling band keratopathy's chemical composition and morphology thus providing insight to the mechanism of formation and allowing for mass production of the material furthering the advances of therapeutic targeting CBK. Our study is the first to demonstrate that low molecular silicon can assist in the formation of CBK. Given the predominance of calcium and presence of silicon in CBK material, we have investigated the effect of calcium and silicon chelators on our reference and synthetic samples. Our results reveals nitrilo-*tris*(methylene) phosphonic acid, citric acid, and fructose as promising choices for chelation therapy for band keratopathy.

The unique structural, physical, and photo-, electro-chemical properties of buckminsterfullerene C<sub>60</sub> and its derivatives have rendered them particularly interesting for the field of nanomedicine. Toward this end, we have synthesized and investigated a series of derivatized C<sub>60</sub> fullerenes possessing amine and amino acid pendant groups as

inhibitors of the zinc enzymes carbonic anhydrases (CAs) and the human immunodeficiency virus type I aspartic protease (HIV-1 PR). Computational studies were performed in order to shed light in understanding the inhibition mechanism of CAs by these derivatives. Our collaborative investigation reveals that the CA isoforms show diverse inhibition profiles with our fullerene derivatives. Both computational and experimental techniques confirmed anti HIV-1 PR inhibitory effects of our C<sub>60</sub> derivatives. Additionally, we have synthesized a series of C<sub>60</sub> fullerene-peptides in order to investigate their cellular uptake, interference *in vitro* with specific DNA binding and inhibition of neuroblastoma cell growth. Our *in vitro* cell studies show that these fullerene-peptides are capable of penetrating into cytoplasm of the JF neuroblastoma cells. Cell viability study was undertaken in order to examine the biological response of our fullerene peptides for neuroblastoma cell proliferation.

“To laugh often and much; to win the respect of intelligent people and the affection of children; to earn the appreciation of honest critics and endure the betrayal of false friends; to appreciate beauty; to find the best in others; to leave the world a bit better, whether by a healthy child, a garden patch or a redeemed social condition; to know even one life has breathed easier because you have lived. This is to have succeeded.”

Ralph Waldo Emerson

## **Acknowledgements**

I would like to express my sincerest of gratitude to my professor Dr. Andrew Barron for the excellent guidance, thoughtful inputs and cordial milieu that he provided me throughout my program at Rice University. I would also like to place on record my thankfulness and appreciation to my committee members Prof. Lon Wilson, Prof. Mason Tomson, and Dr. Marshall Hamill for their invaluable contributions and painstaking effort in going through this manuscript. Special thanks go to Dr. Jianhua Yang of Baylor College of Medicine, Dr. Serdar Durdagi, Dr. Thomas Mavromoustakos, Dr. Manthos Papadopoulos with the National Hellenic Research Foundation and Dr. CIlaudiu Supran of University of Florence for their productive collaboration.

Thanks to all the members of the Barron group for helping me on countless number of occasions, academically and personally, and I wish you and your families all the very best. To Dr. Jianzhong Yang and Carissa Manrique who helped me immensely in getting started and progress with this study, I thank you.

To the wonderful faculty, particularly Dr. Mary McHale and staff, especially Jane McNeal, thank you for making my experience at Rice a wonderful one. I would also like to thank the staff of Shared Equipment Authority, Angelo, Bo, Rich and Wenh for their support. Special thanks to Dr. Rolf Arvidson for his dedication and support with the VSI analyses.

I must acknowledge my undergraduate academic advisor, Prof. Ramiro Sanchez, for believing in me and encouraging me to further my education in the field of chemistry. Special thanks to all my friends for their support and friendships.

Finally, thank you to my parents for making my education as the top priority of their life and to my sisters for their love and moral support. I could not have made it without you. Mehdi, thank you for our two beautiful daughters and for being with me through thick and thin. Sara and Sahar, thanks for all the love and support I could ever

ask for and more. I hope you both know that I recognize the sacrifices you have made to help me get through graduate school.

*Dedicated to my dear parents and beautiful daughters*

## Table of Contents

Introduction	1
<b>Chapter 1. Synthesis of an <i>In-vitro</i> Model System and Therapeutics Studies for Calcific Band Keratopathy Precipitate</b>	
Introduction	14
Results and Discussion	19
Conclusions	47
Experimental	52
References	54
<b>Chapter 2. Biological Effects of Functionalized Buckminsterfullerene (C<sub>60</sub>)</b>	
Introduction	56
Results and Discussion	60
Conclusions	78
Experimental	79
References	81

## List of Figures

### Introduction

- Figure I.1.** External appearance of CBK in the eye. Image is courtesy of Dr. Hamill of Cullen Eye Institute at Baylor College of Medicine. 1
- Figure I.2.** Schematic represents the role of functionalized fullerenes as important nanomaterials in biomedical applications. 4
- Figure I.3.** Molecular structure of C<sub>60</sub> (a) and the related bond length (b). 5
- Figure I.4.** Molecular modeling image of the HIV-1 protease. Color coding is as follows. Yellow: Leu, Ile, Phe, Tyr, Val, Trp, Pro, Gly, Ala. Blue: Lys, Arg. Red: Asp, Glu. Cyan: Thr, Ser, Gln, Asn, Cys, Met, His. The C<sub>60</sub> is colored magenta. 7
- Figure I.5.** Structure of Gd@C<sub>60</sub>. 8

### Chapter 1

- Figure 1.1.** Schematic representation of the reaction between phosphonic acid and calcium carbonate: (a) surface etching and dissolution of calcium carbonate by phosphonic acid, (b) formation of soluble calcium phosphonate complex. 16
- Figure 1.2.** Arrangement of two oxolanediolato ligands at a hydroxosilicon center. 18
- Figure 1.3.** High-resolution XP spectra for eye sample **P2** (a) Ca2p<sub>3/2</sub> and (b) Si2p. 21
- Figure 1.4.** Raman spectrum of human eye sample **P1** showing peaks associated with various silicates. 22
- Figure 1.5.** SEM image of eye samples **P1** (a) and **P2** (b) revealing small fused spherical shapes ~1 - 3 μm in size. The samples were taken from



human patients at Baylor College of Medicine.	23
<b>Figure 1.6.</b> SEM images of calcium silicate grown in the presence of (a) SDS (sample 1) and (b) fumed silica (sample 2) showing the presence of typical crystallites of $\text{CaCO}_3$ .	26
<b>Figure 1.7.</b> SEM image of sample 3 showing the presence of fused spherical features in a matrix.	27
<b>Figure 1.8.</b> Plot of sphere size as a function of Si:Ca ratio for eye samples P1 and P2 in comparison with synthetic samples 3 and 20.	28
<b>Figure 1.9.</b> SEM images of samples prepared with (a) 4x the silica (sample 4) and (b) $\frac{1}{2}$ x the silica (sample 6) as compared to sample 3.	31
<b>Figure 1.10.</b> SEM image of sample 7 formed using silicic acid.	32
<b>Figure 1.11.</b> SEM images of sample 10 formed using silicone oil as the silicon source.	33
<b>Figure 1.12.</b> SEM images of sample 13 .	35
<b>Figure 1.13.</b> SEM images of (1) sample 14 and (b) sample 15 showing the effect of adding a non-polar compounds (hexane) to the calcium/silica reaction.	37
<b>Figure 1.14.</b> SEM images of (a) sample 16, and (b) sample 17 showing the formation of very small non-fused spheres with the addition of hexane and dodecane, respectively.	37
<b>Figure 1.15.</b> SEM image of sample 19.	38
<b>Figure 1.16.</b> SEM images of sample 20 showing the formation of highly fused spheres.	39
<b>Figure 1.17.</b> Raman spectra of sample 20.	40
<b>Figure 1.18.</b> High-resolution XP spectra of sample 20 (a) $\text{Ca}2p_{3/2}$ and (b) $\text{Si}2p$ .	41

- Figure 1.19.** VSI maps of sample **20** surface (80X objective) showing the initial surface (a), and reaction sequence of this surface exposed to H<sub>6</sub>ntmp solution at 15 min (b), 30 min (c), and 1 h (d). 44
- Figure 1.20.** VSI maps of sample **20** surface (10x objective) of the initial surface (a) and reaction of this surface exposed to citric acid solution at 1 min while removing solvent (b), at 1 min. after solvent removal (c). 45
- Figure 1.21.** VSI maps of sample **20** surface (80X objective) of the initial surface (a), and reaction sequence of this surface exposed to fructose solution at 1 h (b), and 3 h (c). 46
- Figure 1.22.** <sup>31</sup>P NMR spectra of H<sub>6</sub>ntmp solution (a) and its reactions with 2 mg (b), 6 mg (c), 10 mg (d), and 14 mg (e) of CaCO<sub>3</sub>. 48
- Figure 1.23.** <sup>31</sup>P NMR spectra of H<sub>6</sub>ntmp solution (a) and its reactions with 2 mg (b), 4 mg (c), 8 mg (d), and 16 mg (e) of sample 20. 49
- Figure 1.24.** IR of citric acid and citric acid complex. 50

## Chapter 2

- Figure 2.1.** Active site of  $\alpha$ -CA enzymes (Zn<sup>2+</sup> is shown as a pink sphere and histidines in green). 59
- Figure 2.2.** Compounds synthesized for HIV-1 P and CAs inhibition studies. 60
- Figure 2.3.** The binding interactions of compound **2.1** with (S) configuration at \*C1 with the active site residues of HIV-1 P. 63
- Figure 2.4.** The binding interactions of compound **2.1** with (R) configuration at \*C1 with the active site residues of HIV-1 P. 64
- Figure 2.5.** The binding interactions of compound **I** with the active site residues of HIV-1 P. 65

- Figure 2.6.** Binding of fullerene **2.1** to hCA II (shown as ribbon representation of the amide backbone). The catalytic Zn(II) ion is the yellow sphere at the center of the molecule. 68
- Figure 2.7.** Binding of fullerene **2.5** to hCA II as obtained by the induced fit docking method. Yellow and green dashed bonds show H-bonds and close-van der Waals contacts, respectively. The catalytic Zn(II) ion is shown as orange spheres. 70
- Figure 2.8.** Binding of compound **2.3** to hCA IX. Yellow and green dashed bonds show H-bonds and close-van der Waals contacts, respectively. The catalytic Zn(II) ion is shown as the yellow sphere. 71
- Figure 2.9.** Superimposition of hCA II (shown in yellow colored ribbons) and hCA IX (shown in green colored ribbons) docking complexes of fullerene **2.3**. Dark colored fullerene shows the binding pose at hCA II and light colored fullerene shows the binding pose at hCA IX. The Zn(II) ion is shown by yellow (for hCA II) and green (for hCA IX) sphere, respectively. 72
- Figure 2.10.** The basic helix-loop-helix/leucine zipper of Myc family proteins. 73
- Figure 2.11.** Fluorescence images of JF cell incubated with (a) F-K(FITC)-NDLRSAFATLRDHV and (b) Baa-K(FITC)-NDLRSAFATLRDHV. 75
- Figure 2.12.** Inhibition of fullerene peptides against the proliferation of neuroblastoma cell line (SH-SY5Y), (**2.10**, ●), (**2.11**, ●), and (**2.12**, ○). 76
- Figure 2.13.** Inhibition of fullerene peptides against the proliferation of neuroblastoma cell line (SH-SY5Y), (**2.9**, ●), (**2.10**, ●), and (**2.11**, ○). 76

- Figure 2.14.** IMR-32 neuroblastoma cell line proliferation in DMSO, and Baa-peptides **2.10** and **2.12**. 77
- Figure 2.15.** LAN-1 neuroblastoma cell line proliferation in DMSO, and Baa-peptides **2.10** and **2.12**. 77
- Figure 2.16.** LAN-1 neuroblastoma cell line proliferation in DMSO, and Baa-peptides **2.10** and **2.12**. 78

## List of Tables

### Chapter 1

- Table 1.1.** Summary of XPS data for eye samples and selected synthetic samples. 20
- Table 1.2.** The Si:Ca ratios as determined by XPS and sphere sizes as determined by SEM of selected samples. 24
- Table 1.3.** Summary of reaction conditions for the formation of CBK model materials in the absence of hydrocarbon. 25
- Table 1.4.** Selected binding energies obtained from high resolution XPS data. 30
- Table 1.5.** Summary of reaction conditions for the formation of CBK model materials in the presence of hydrocarbon. 36

### Chapter 2

- Table 2.1.** Comparison of experimental and computational binding energies the fullerene derivatives at HIV-1 P. 62
- Table 2.2.** Inhibition of mammalian carbonic anhydrase isozymes with fullerene derivatives. 66
- Table 2.3.** Computational binding energies of fullerene derivatives to CA II and CA IX. 69
- Table 2.4.** Peptide sequences and cell lines studied. 74

## Abbreviations

Baa	Bucky amino acid, fullerene phenylalanine
Boc	<i>tert</i> -butyloxidencarbonyl, $-\text{C}(\text{O})\text{OC}(\text{CH}_3)_3$
C <sub>60</sub>	Buckminsterfullerene, [60] fullerene
°C	degree centigrade
<i>ca.</i>	circa, approximately
CBK	calcific band keratopathy
°	degree
δ	delta, chemical shift (NMR)
DNA	deoxyribonucleic acid
EQ	equation
eV	electron volt
FITC	fluorescein isothiocyanate
H	hour
HPLC	high-performance liquid chromatography
Hz	hertz
<i>i.e.</i>	<i>id est</i> , that is (to say)
IR	infrared spectroscopy
kJ	kilo joule
mg	milligram(s), $10^{-3}$ g
μL	microliter(s), $10^{-6}$ L
μm	micrometer(s), $10^{-6}$ m
μM	micromolar, $10^{-6}$ M
mL	milliliter(s), $10^{-3}$ L
MS	mass spectrometry
min	minute(s)

MALDI-MS	matrix-assisted laser desorption ionization mass spectroscopy
nm	nanometer, $10^{-9}$ m
NMR	nuclear magnetic resonance spectroscopy
ppm	part per million
SEM	scanning electron microscopy
VSI	vertical scanning interferometry
XPS	X-ray photoelectron spectroscopy

## Introduction

**Band Keratopathy.** Calcific band keratopathy (CBK), first named by Dixon in 1848 as a “calcareous film of the cornea”, refers to the usually slow and gradual accumulation of calcific minerals in a band shape limited to the exposed interpalpebral zone of the cornea (Figure I.1).<sup>1,2</sup> This condition generally appears as a variably dense opacification of the peripheral cornea that spreads with time into the central cornea. The deposited material is a non-crystalline form of calcium deposited in the superficial layers of the cornea.<sup>3</sup> It is known that the initial stages of precipitation occur in Bowman’s layer, the basement membrane of the corneal epithelium.<sup>4</sup> Holes in the calcific band are present where the corneal nerves penetrate the Bowman’s membrane resulting in a picture that resembles “Swiss cheese”.<sup>5,6</sup>

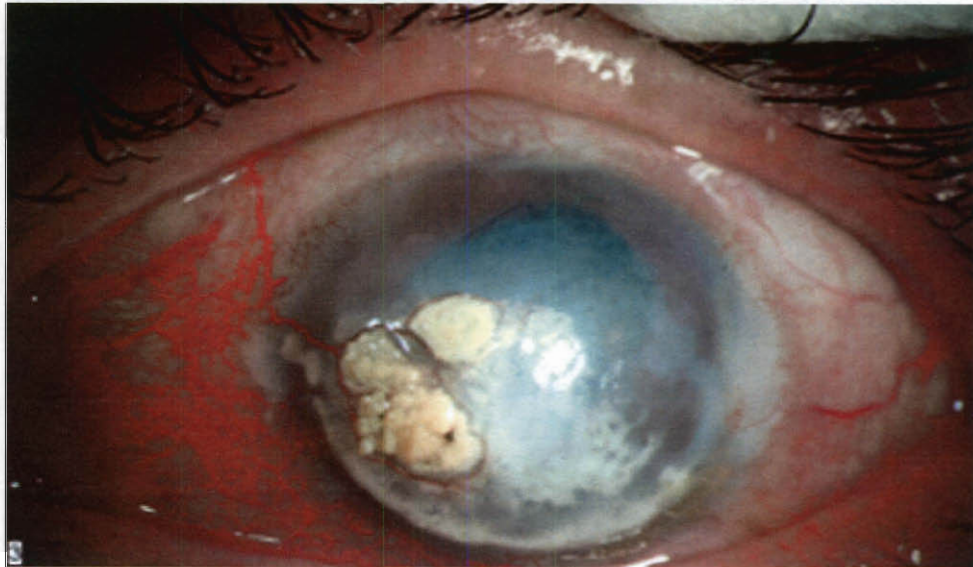


**Figure I.1.** External appearance of CBK in the eye. Image is courtesy of Dr. Hamill of Cullen Eye Institute at Baylor College of Medicine.

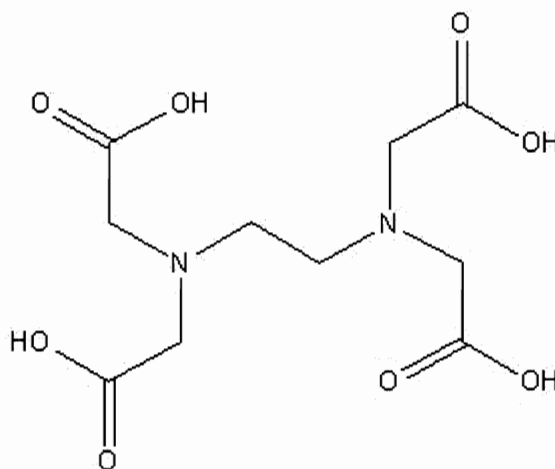


While the initial stages of CBK are asymptomatic, as it progresses epithelial defects and surface irregularities can develop. The usual presenting symptoms of CBK are ocular pain and photophobia due to corneal epithelial erosions and decreased vision or even blindness resulting from opacification of the cornea.<sup>7</sup>

CBK can occur in the setting of a variety of chronic ocular or systemic diseases such as end stage glaucoma and chronic intraocular inflammation (e.g., juvenile rheumatoid arthritis).<sup>8,9,10</sup> Multiple case reports suggest an association between development of CBK and use of oils in endothelial touch during retinal surgery.<sup>11,12,13</sup> Despite all the existing experimental and clinical reports for CBK, little is thus far known about the pathogenesis and etiology of this condition. Development of a model system *in-vitro* can be very useful in understanding the pathology and chemistry of CBK and most importantly, in exploration of therapeutic targeting of CBK.

Treatment alternatives for this condition are limited. Palliative options include simple lubrication and the use of bandage contact lenses for comfort. In some mild cases this approach may be satisfactory. For more advanced cases these treatments become ineffective and surgical intervention to debulk the calcific deposits and a restoration of the corneal surface is required. Surgical approaches to remove the calcific deposits include surgical keratectomy with a blade or burr, excimer laser photokeratectomy, and chemical chelation. These treatment options are less than satisfactory as they are frequently associated with significant post treatment pain, discomfort, and a delay in visual recovery.<sup>14</sup> In addition, keratectomy by any method results in loss of corneal tissue and surface irregularity. The metal complexing agent ethylenediaminetetraacetic acid (EDTA, I) has been found to provide some benefit by softening the CBK precipitate allowing for easier removal. However, this treatment is far from ideal given that EDTA is not specific to calcium and can potentially bind to any metal, therefore, causing adverse side effects. Unfortunately none of these treatments address the causative factors or

prevent further calcium deposition. In order to better treat this condition, a more efficient method of breaking-up or dissolving the CBK precipitate without disrupting the corneal tissue or disturbing the surface anatomy is desirable. More importantly, perhaps, is the need to develop a treatment approach to prevent the deposition in the first place thus treatment alternatives that can prevent CBK from forming also need to be studied. In order to accomplish this goal it is necessary to better understand the chemical conditions that promote the formation of the CBK precipitate. Chapter 1 of this thesis describes a systematic investigation towards formation of precipitates mimicking the calcium materials of CBK. It also details the use of various chemical extractors and their medicinal effect on our synthetic material.



(I)

### **C<sub>60</sub>-based nanomaterials for enzyme inhibition and DNA binding.**

Nanomedicine, an important branch of nanotechnology, has emerged as a new field of research for diagnostics and therapeutics. The field of nanomedicine refers to highly specific design and development of nanomaterials at the molecular scale for identifying and curing diseases. Multifunctional liposomal nanoparticles, functionalized fullerenes,

functionalized nanotubes, iron oxide nanoparticles, polymeric micelles, dendrimers, nanoshells, and polymeric microspheres are amongst the investigated nanomaterials in the field of medicine (Figure I.2).<sup>15</sup>

Functionalized C<sub>60</sub> fullerenes have become an important member of the rapidly growing nanomedicine family. This is due to the unique physical, chemical, optical and electronic properties of the C<sub>60</sub> nanosphere core. These derivatives have shown enzyme inhibition, anticancer, antibacterial, cell signaling, DNA and genomic activities, photodynamic activation, and antioxidant properties.

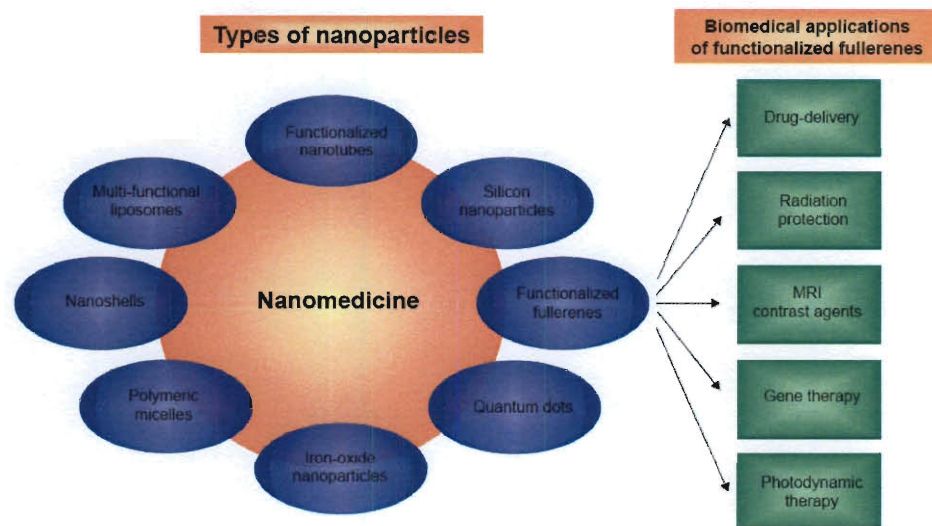


**Figure I.2.** Schematic represents the role of functionalized fullerenes as important nanomaterials in biomedical applications.<sup>15</sup>

Buckyball or buckminsterfullerene (C<sub>60</sub>) consists of 60 carbon atoms arranged in the form of a truncated icosahedron with 12 pentagonal faces which are fully surrounded by 20 hexagonal faces (Figure I.3).<sup>16</sup> Each carbon atom is bonded to three others and is sp<sup>2</sup> hybridized. Buckminsterfullerene (C<sub>60</sub>) has two bond lengths: the [6-6] ring bonds between two hexagons which due to their considerably higher double-bond

characteristics are shorter than the [6-5] ring bonds between a hexagon and a pentagon.<sup>17</sup> The diameter of this molecule is 0.7 nm.<sup>17</sup>

Although pristine C<sub>60</sub> is sufficiently soluble in carbon disulfide and in aromatic or chlorinated hydrocarbons, it is sparingly soluble or aggregates easily in many other organic solvents and it is virtually insoluble in polar solvents and aqueous media. This great obstacle hampers the practical applications of this molecule, especially its biological applications.<sup>18,19</sup> Therefore, the covalent functionalization of C<sub>60</sub> has been explored vigorously in order to overcome this hurdle and to a great extent has solved the problem.<sup>20,21,22,23</sup> These explorations have allowed the preparation of highly soluble C<sub>60</sub> derivatives while preserving the unique physical, chemical, optical and electronic properties of the C<sub>60</sub> core. Therefore, the research for potential applications of these water-soluble fullerene derivatives in medicinal chemistry has been significantly increased in recent years.

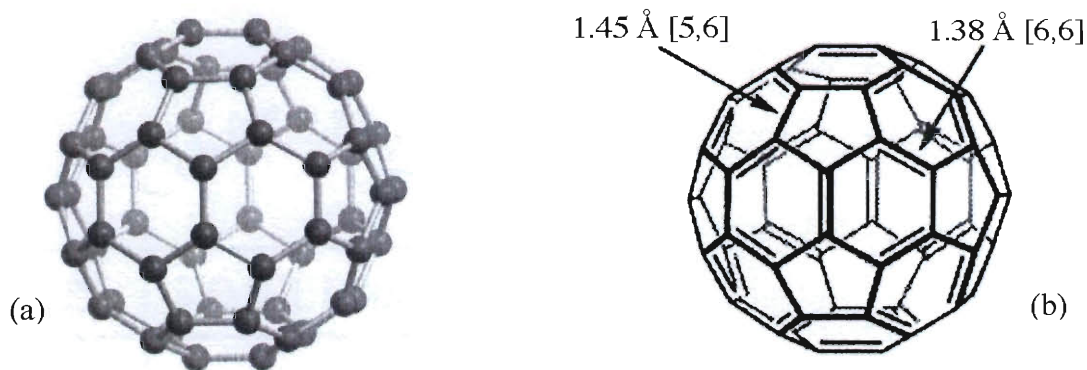


**Figure I.3.** Molecular structure of C<sub>60</sub> (a) and the related bond length (b).

With a diameter of about 1 nm, which is the same as the opening of the active site entrance or the interface of subunits of many enzymes, C<sub>60</sub> spheroid has become an

appealing candidate for enzyme inhibition studies.<sup>24,25</sup> One of the first applications of biologically active C<sub>60</sub> was proposed by Friedman *et al.* in 1993 (Figure I.4).<sup>26</sup> By means of molecular modeling, they proposed that C<sub>60</sub> and its derivatives can be inhibitors of HIV-1 protease (HIV-1 P) due to their complementary fit with the hydrophobic cavity of the enzyme. Their subsequent *in-vitro* studies with a series of water soluble fullerene derivatives confirmed the inhibition effects of these derivatives in the low micromolar concentration range.<sup>27</sup> Other researchers have studied anti HIV-1 P activity of a variety of fullerene derivatives since then showing similar inhibition results.<sup>24</sup>

The unique hollow space inside of the C<sub>60</sub> fullerene cage has attracted wide interest for incorporation of metal ions resulting in a novel form of fullerene-based material labeled endohedral metallofullerenes.<sup>24</sup> This new class of fullerenes are particularly interesting because of their promising applications in the field of nuclear medicine.<sup>28,29</sup> The major disadvantage of the current radiopharmaceutical drugs containing chelated radioisotopes of metals used in radiomedicine and diagnostic radiology is their *in-vivo* kinetic instability which can allow the release of small quantities of toxic radiomaterials.<sup>30</sup> In an endohedral metallofullerene, the metal is placed in the fullerene cage and has no chance of escaping out providing a distinct advantage over the current metal chelate complexes (Figure I.5). Wilson and colleagues have been the pioneers in the pursuit of utilizing holmium and gadolinium containing metallofullerenes as new therapeutic and magnetic resonance imaging (MRI) contrast agents.<sup>31,32</sup> Their studies have revealed that metallofullerenes can act as radiotracers and as contrast enhancing agents for magnetic resonance imaging (MRI) with fundamental advantages over commercially-available chelate compounds with respect to improved physiological stability and lack of acute toxicity.

Besides the striking size and geometric features, C<sub>60</sub> also demonstrate a variety of interesting photophysical properties. The extended  $\pi$ - conjugation of the fullerene cage

allows it to transition from a short-lived singlet excited state to a long-lived triplet excited state upon irradiation with visible or UV light generating reactive oxygen species (ROS).<sup>33,34</sup> These reactive oxygen species (ROS) react with a wide range of biological targets and are known to be involved in both cellular signaling and cell damaging. On the other hand, it has been also reported that C<sub>60</sub> can function as a “free radical sponge” and quench various free radicals more efficiently than conventional antioxidants due to the delocalized  $\pi$  double bond system of the fullerene cage.<sup>35,36</sup> This unique dual nature of C<sub>60</sub> fullerene and its derivatives to either quench or generate ROS has rendered them as promising candidates for a variety of biological applications including: DNA photo-cleavage,<sup>37</sup> photodynamic therapy (PDT),<sup>38</sup> neuroprotection,<sup>39,40</sup> antimicrobial and antiapoptotic activities.<sup>41,42</sup>

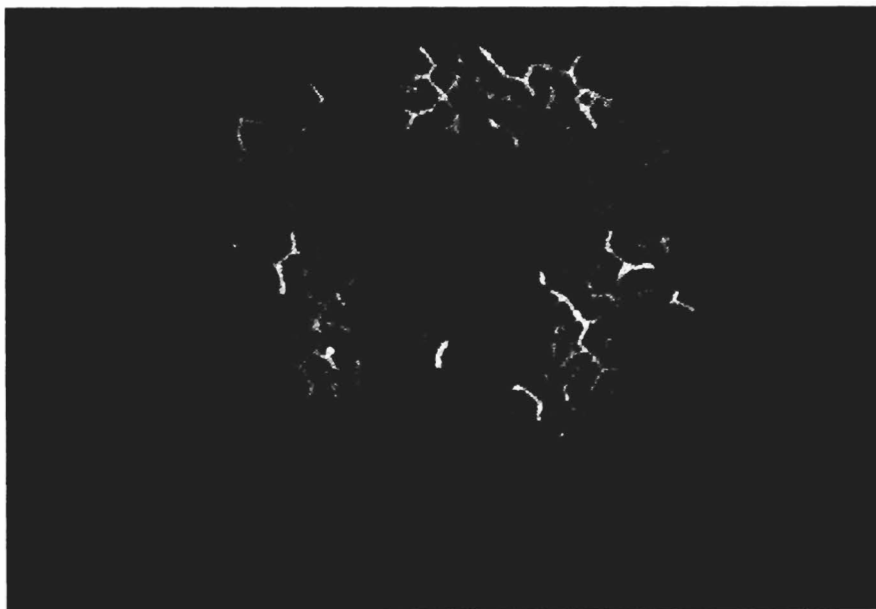


**Figure I.4.** Molecular modeling image of the HIV-1 protease. Color coding is as follows. Yellow: Leu, Ile, Phe, Tyr, Val, Trp, Pro, Gly, Ala. Blue: Lys, Arg. Red: Asp, Glu. Cyan: Thr, Ser, Gln, Asn, Cys, Met, His. The C<sub>60</sub> is colored magenta.<sup>26</sup>

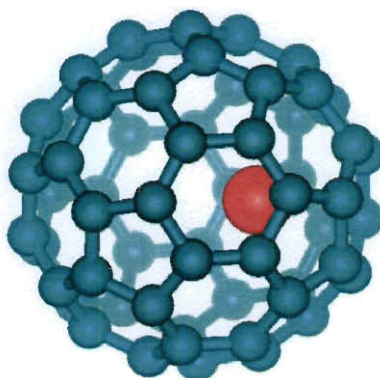


**Figure I.5.** Structure of Gd@C<sub>60</sub>.<sup>43</sup>

Hydrophobicity is another important property of C<sub>60</sub> which has been utilized in design of novel compounds for potential applications in drug, peptide, protein and gene delivery into living cells for therapeutic purposes.<sup>44,45,46,47,48,49</sup> Paclitaxel is regarded as one of the most promising drugs against lung cancer with a cytotoxicity more dependent on its exposure time than its increased concentration.<sup>44</sup> A fullerene-paclitaxel conjugate designed by Wilson and colleagues to slowly release the drug for aerosol liposome delivery of paclitaxel. This slow-release drug-delivery system showed significant anticancer activity in tissue culture. Our group has previously reported a novel approach to formation of cell penetrating peptides using fullerene-peptide conjugates. We have demonstrated that the hydrophobic fullerene core plays an important role in the delivery of these fullerene-peptides to either the cytoplasm or nucleus of the cell.<sup>45</sup> Functionalized C<sub>60</sub> fullerenes have also been explored as transfection vectors to deliver exogenous DNA into cells and their ability to mediate gene transfer has been tested.<sup>47</sup> It is known that the DNA-binding ability of a molecule depends both on its hydrophobicity and cationic charge and the binding becomes stronger as the molecule becomes more hydrophobic and more cationic.<sup>50</sup> Aminofullerenes have shown to effect transfection with an efficiency as high as the common lipid-based transfection agents.

In addition to the foregoing described potential medicinal applications of functionalized C<sub>60</sub> fullerene, there are many other promising investigations for biomedical applications of C<sub>60</sub> fullerene compounds. Functionalized amino acid and peptide based fullerenes have been found to activate enzymes involved in the oxidative deamination of biogenic amines.<sup>46</sup> Fullerene-substituted amino acid incorporated into peptides have shown significant effects on the secondary structures and self assembly of properties of these peptides.<sup>51</sup> Successful selected tissue targeting has been reported using a fullerene-based material.<sup>52</sup> Fullerene and its derivatives are also promising candidate for design of various composite biomaterials.<sup>53</sup>

Research on functionalized C<sub>60</sub> fullerenes has dramatically changed their impact in medicinal chemistry. With creative and collaborative participation of scientists from various disciplines, C<sub>60</sub> fullerene and its derivatives will see many more new biomedical applications that will serve to increase the quality of life. Chapter 2 of this thesis describes our recent achievements in this field with regards to inhibition activities of a series of functionalized C<sub>60</sub> derivatives from our previously synthesized library of fullerene derivatives against HIV-1 protease and carbonic anhydrase isoforms. It also describes the synthesis of a series of novel fullerene-base amino acid peptides for investigation of their cellular uptake and neuroblastoma cell growth inhibition.

## References

- 1 N. B. Kurnick, *Am. J. Dis. Child.*, 1942, **63**,742.
- 2 W. Bowman, *Lectures on the parts of concerned in the operations on the eye, and on the structure of the retina*, 1849.
- 3 M. A. Lemp and R. A. Ralph, *Am. J. Ophthalmol.*, 1977, **83**, 657.
- 4 G. R. O'Connor, *Trans. Am. Ophthalmol. Soc.*, 1972, **70**, 58.



- 5 D. M. Najjar, E. J. Cohen, C. J Rapuano, and P. R. Laibson, *Am. J. Ophthalmol.*, 2004, **137**, 1056.
- 6 J. W. Sowka, A. S. Gurwood, and A. G. Kabat, Band Keratopathy. Handbook of ocular disease management. *Review of Optometry Online*, <http://legacy.revoptom.com/handbook/2007/diseasehandbookkro.pdf>. Accessed September 29, 2008.
- 7 Y. S. Kwon, Y. S. Song, and J. C. Kim, *J. Korean. Med. Sci.*, 2004, **19**, 611.
- 8 D. E. Braverman and W. E. Snyder, *Metab. Pediatr. Syst. Ophthalmol.*, 1987, **10**, 39.
- 9 D. J. Doughman, G. A. Olson, S. Nolan and R. G. Hajny, *Arch. Ophthalmol.*, 1969, **81**, 264.
- 10 M. J. Taravella and S. L. Forstot, *Arch. Ophthalmol.*, 1991, **109**, 1072.
- 11 G. N. Foulks, D. L. Hatchell, A. D. Proia, and G. K Klintworth, *Cornea*, 1991, **10**, 29.
- 12 S. R. Bennett, G. W. Abrams, *Arch Ophthalmol*, 1990, **108**, 1387.
- 13 K. Lemmen, S. Dimopoulos, B. Kirchhof, and K. Heimann, *Dev. Ophthalmol.*, 1987, **13**, 88.
- 14 D. P. S. O'Brart, D. S. Gartry, C. P. Lohmann, A. L. Patmore, M. G. Muir, and J. Marshall, *Br. J. Ophthalmol.*, 1993, **77**, 702
- 15 R. Partha and J. Conyers, *Nanomedicine*, 2009, **4**, 261.
- 16 H. W. Kroto, J. R. Heath, S. C. O'Brien, R. F. Curl, and R. E. Smalley, *Nature*, 1985, **318**, 162.
- 17 F. Diederich and C. Thilgen. *Science*, 1996, **271**, 317.
- 18 R. S. Ruoff, d. S. Tse, R. Malhotra, and D. C. Lorents, *J. Phys. Chem.*, 1993, **97**, 3379.

- 19 N. Sivaraman, R. Dhamodaran, I. Kaliappan, T. G. Srinivassan, P. R. V. Rao, and C. K. Mathews, *J. Org. Chem.*, 1992, **57**, 6077.
- 20 M. Brettreich and A. Hirsch, *Tetrahedron Lett.*, 1998, **39**, 2731.
- 21 R. D. Bolskar, A. F. Benedetto, L. O. Husebo, R. E. Price, E. F. Jackson, S. Wallace, L. J. Wilson, and J. M. Alford, *J. Am. Chem. Soc.*, 2003, **125**, 5471.
- 22 T. Da Ros and M. Prato, *Chem. Commun.*, 1999, **8**, 663.
- 23 A. W. Jensen, S. R. Wilson, and D. I. Schuster, *Bioorg. Med. Chem.*, 1996, **4**, 767.
- 24 N. Tagmatarchis and H. Shinohara, *Mini-Reviews in Medicinal Chemistry*, 2001, **1**, 339.
- 25 D. J. Wolff, D. P. P. Alexandru, K. Mialkowski, C. F. Richardson, D. I. Schuster, and S. R. Wilson, *Arch. Biochem. Biophys.*, 2000, **378**, 216.
- 26 S. H. Friedman, D. L. DeCamp, R. P. Sijbesma, G. Srdanov, F. Wudl, G. and L. Kenyon, *J. Am. Chem. Soc.*, 1993, **115**, 6506.
- 27 R. P. Sijbesma, G. Srdanov, F. Wudl, J. A. Castoro, C. Wilkins, S. H. Friedman, D. L. DeCamp, and G. L. Kenyon, *J. Am. Chem. Soc.*, 1993, **115**, 6510.
- 28 P. P. Fatouros, F. D. Corwin, Z. J. Chen, W. C. Broaddus, J. L. Tatum, B. Kettenmann, Z. Ge, H. W. Gibson, J. L. Russ, A. P. Leonard, J. C. Duchamp, and H. C. Dorn, *Radiology*, 2006, **240**, 756.
- 29 B. Sitharaman, L. A. Tran, Q. P. Pham, R. D. Bolskar, R. Muthupillai, S. D. Flamm, A. G. Mikos, and L. J. Wilson, *Contrast Media Mol. Imaging.*, 2007, **2**, 139.
- 30 D. W. Cagle, S. J. Kennel, S. Mirzadeh, M. J. Alford, and L. J. Wilson, *Proceedings of the National Academy of Sciences of the United States of America*, 1999, **96**, 5182.
- 31 D. W. Cagle, T. P. Thrash, M. Alford, L. P. F. Chibante, G. J. Ehrhardt, and L. J. Wilson, *J. Am. Chem. Soc.*, 1996, **118**, 8043.

- 32 B. Sitharaman and L. J. Wilson, *J. Biomed. Nanotech.*, 2007, **3**, 342.
- 33 J. A. Arbogast, A. P. Darmany, C. S. Foote, F. N. Diederich, R. L. Whetten, Y. Rubin, M. M. Alvarez, and S. J. Anz, *J. Phys. Chem.*, 1991, **95**, 11.
- 34 D. M. Guldi and M. Prato, *Acc. Chem. Res.*, 2000, **33**, 695.
- 35 P. J. Krusic, E. Wasserman, P. N. Keizer, J. R. Morton, and K. F. Preston, *Science*, 1991, **254**, 1183.
- 36 J. J. Yin, F. Lao, P. P. Fu, W. G. Warmer, Y. Zhao, P. C. Wang, Y. Qiu, B. Sun, G. Xing, J. Dong, X. Liang, and C. Chen, *Biomaterials*, 2009, **30**, 611.
- 37 H. Tokuyama, S. Yamago, E. Nakamura, T. Shiraki, and Y. Sugiura, *J. Am. Chem. Soc.*, 1993, **115**, 7918.
- 38 P. Mroz, G. P. Tegos, H. Gali, T. Wharton, T. Sarna, and M. R. Hamblin, *Photochem. Photobiol. Sci.*, 2007, **6**, 1139.
- 39 L. L. Dugan, D. M. Turetsky, C. Du, D. Lobner, M. Wheeler, C. R. Almlie, C. K. Shen, T. Y. Luh, D. W. Choi, and T. S. Lin, *Proc. Natl. Acad. Sci. USA*, 1997, **94**, 9434.
- 40 M. Bisaglia, B. Natalini, R. Pellicciari, E. Straface, W. Malorni, D. Monti, C. Franceschi, and G. L. Schettini, *J. Neurochem.*, 2000, **74**, 1197.
- 41 T. Da Ros, M. Prato, F. Novello, M. Maggini, and E. Banfi, *J. Org. Chem.*, 1996, **61**, 9070.
- 42 L. L. Dugan, D. M. Turetsky, C. Du, D. Lobner, M. Wheeler, C. R. Almlie, C. K.-F. Shen, T.-Y. Luh, D. W. Choi, and T.-S. Lin, *Proc. Natl. Acad. Sci. U.S.A.*, 1997, **94**, 9434.
- 43 R. F. Sabirianov, W. N. Mei, J. Lu, Y. Gao, X. C. Zeng, R. D. Bolskar, P. Jeppson, N. Wu, A. N. Caruso, and P. A. Dowben, *J. Phys. Cond. Matt.*, 2007, **19**, 082201/1.

- 44 T. Y. Zakharian, A. Seryshev, B. Sitharaman, B. E. Gilbert, V. Knight, and L. J. Wilson, *J. Am. Chem. Soc.*, 2005, **127**, 12508.
- 45 R. Partha, L. R. Mitchell, J. L. Lyon, P. P. Joshi, and J. L. Conyers, *ACS Nano.*, 2008, **2**, 1950.
- 46 J. Yang, K. Wang, J. Driver, J. Yang, and A. R. Barron, *Org. & Biomol. Chem.*, 2007, **5**, 260.
- 47 A. Bianco, T. Da Ros, M. Prato, and C. Toniolo, *J. Pep. Sci.*, 2001, **7**, 208.
- 48 E. Nakamura, H. Isobe, N. Tomita, M. Sawamura, S. Jinno, and H. Okayama, *Angew. Chem. Int. Ed.*, 2000, **39**, 4254.
- 49 H. Isobe, N. Tomita, S. Jinno, H. Okayama, and E. Nakamura, *Chem. Lett.*, 2001, 1214.
- 50 H. Isobe, W. Nakanishi, N. Tomita, S. Jinno, H. Okayama, and E. Nakamura, *Chem. Asian J.*, 2006, **1**, 167.
- 51 J. Yang, L. B. Alemany, J. Driver, J. D. Hartgerink, and A. R. Barron, *Chemistry*, 2007, **13**, 2530.
- 52 K. A. Gonzalez, L. J. Wilson, W. Wu, and G. H. Nancollas, *Bioorg. Med. Chem.*, 2002, **10**, 1991.
- 53 J. C. Lin and C. h. Wu, *Biomaterials*, 1999, **20**, 1613.

## Chapter 1

# Synthesis of an *In-vitro* Model System and Therapeutics Studies for Calcific Band Keratopathy Precipitate

### Introduction

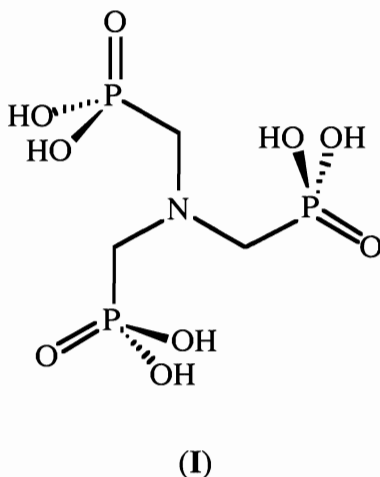
It is well known that calcific band keratopathy is the result of precipitation of calcium salts on the corneal surface (directly under the epithelium), and that serum and normal body fluids (e.g., tears) contain calcium in concentrations that approach their solubility product; however, this does not explain what factors promote precipitation in some subjects and not in others. Is there an external trigger that promotes the formation of the CBK precipitate? Since CBK is a rare disease and none of the *in-vivo* studies thus far have been able to identify the cause and pathogenesis of CBK, development of an *ex-situ* model system, heretofore unavailable, would be of obvious importance for shedding light into the mysteries behind formation of this disease.

In addition, biological samples of band keratopathy deposits are very small making experimentation to test new therapies difficult if not impossible. Given the limited quantities recoverable from treatment of band keratopathy (1 - 5 mg) it would be desirable to have a model material on which potential complexing/digestion agents can be tested. To be successful this material must be easily produced for further testing, and also allow an understanding of the factors involved in the formation of CBK material in the human eye.

In this regard we have characterized samples from individual patients by scanning electron microscopy (SEM), X-ray photoelectron spectroscopy (XPS), and X-ray diffraction (XRD) and Raman spectroscopy with a view to replicate its structure, morphology, and composition in an easily prepared model analog. In designing the model

material we have considered some of the environmental conditions and exposures that promote CBK.

Conventional treatments are limited and do not address the basic pathophysiology of the condition. Given the predominance of calcium in CBK material it would be reasonable to expect that one form of treatment would involve the specific complexation and dissolution of calcium. Complexation of calcium from solid materials has been extensively studied with regard to the processes that control cement setting and retarding.<sup>1</sup> In this regard, the Barron research group has previously reported that cement retarders used in the oil industry, such as phosphonic acids in particular, nitrilotris(methylene)phosphonic acid,  $N[CH_2PO(OH)_2]_3$  ( $H_6ntmp$ , **I**), are highly effective at the extraction of calcium from cementitious minerals.<sup>2,3</sup>



The initial steps of the proposed mechanism of action for the phosphonic acid with the calcium mineral surface are shown schematically in Figure 1.1. It is possible that a similar mechanism could occur for calcium chelation in the eye with  $H_6ntmp$  or a similar calcium chelator. The complexation will allow the calcium to become soluble, therefore able to wash out in solution. The calcium complex could either be excreted

through the nasolacrimal duct into the nose which leads either to the maxillary sinus or the throat or the solution can expelled out of the eye directly. Therefore,  $H_6ntmp$  was chosen for our calcium complexation studies for the synthetic samples.

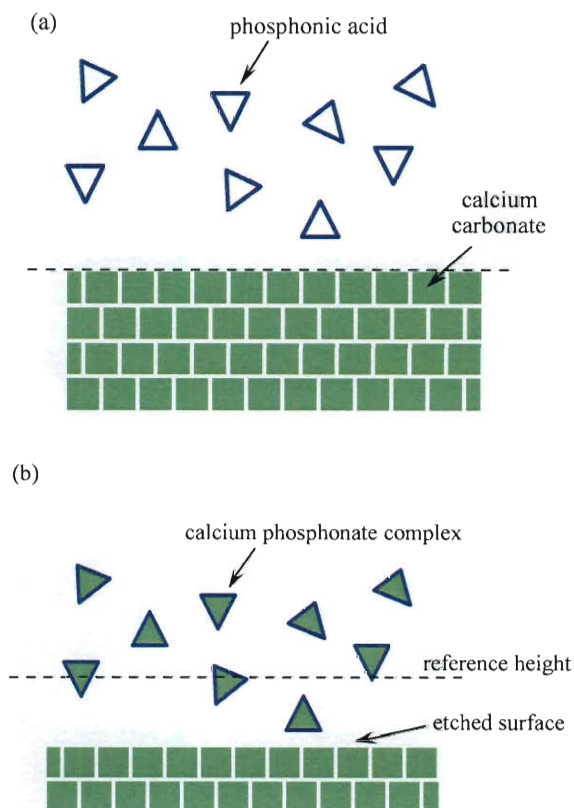
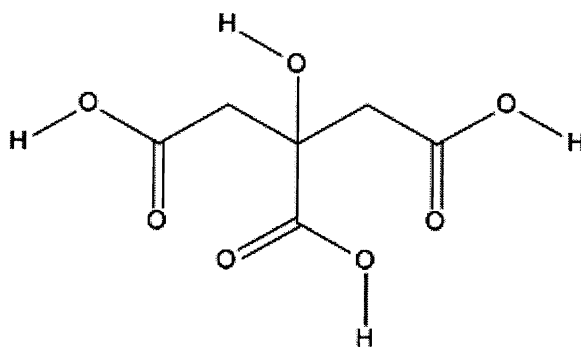


**Figure 1.1.** Schematic representation of the reaction between phosphonic acid and calcium carbonate: (a) surface etching and dissolution of calcium carbonate by phosphonic acid, (b) formation of soluble calcium phosphonate complex.<sup>3</sup>

As an alternative to the phosphate ligands, study of other extracting agents, such as citric acid (**II**), to help prevent the growth of CBK is of great interest. Citric acid is a promising choice for chelation therapy for band keratopathy, since it is naturally produced in the body to complex with excess calcium in the kidneys to avoid the

formation of kidney stones.<sup>4,5</sup> It could thus be an ideal molecule to utilize for CBK treatment. One drawback in using citric acid is that it can be harmful to the eye; therefore, a very low concentration will be used to assure the patient's safety. Citric acid has been studied to reduce corneal ulcers in alkali eye burns. A 10% citrate solution was used to treat eyes and no major negative side effects occurred in the eyes of the patients.<sup>6</sup> Therefore, we believe that citric acid at a 10% or lower concentration will remain safe to the patients.



(II)

The possibility of treatment is further complicated by our findings that human sourced samples of band keratopathy material contain significant concentrations of silicon in the form of a calcium silicate.<sup>7</sup> The hydration of calcium silicate minerals to form hydrated silicates is what gives cement its strength. Therefore, we believe excess silicon could also be a cause for CBK and chelation therapy could decrease the probability of its formation. This further suggests that silicon chelators may be viable treatments. A possible solution for silicon chelation is incorporating the use of monosaccharides. They are inexpensive and readily available; so they qualify as a good practical candidate. Also, monosaccharides are naturally occurring in the vitreous humor



of the eye, so they should not be harmful to patients and they are representative of the conditions within the eye.<sup>8</sup> When silicon is chelated to sugar, it forms a five coordinate *syn* species, Figure 1.2.<sup>9</sup> The 1,2 diol group with the anomeric hydroxyl is needed to form the *cis*-isomer for the chelating reaction to occur. The *cis*-conformation is able to occur if the stability constant is more than the isomerization energy.

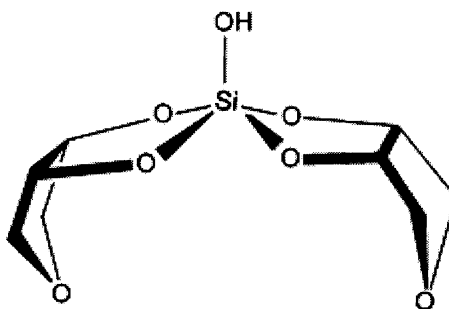
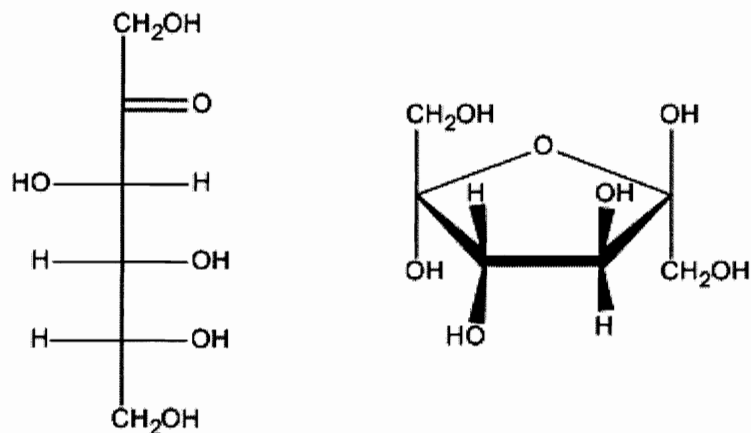


**Figure 1.2.** Arrangement of two oxolanediolato ligands at a hydroxosilicon center.<sup>9</sup>

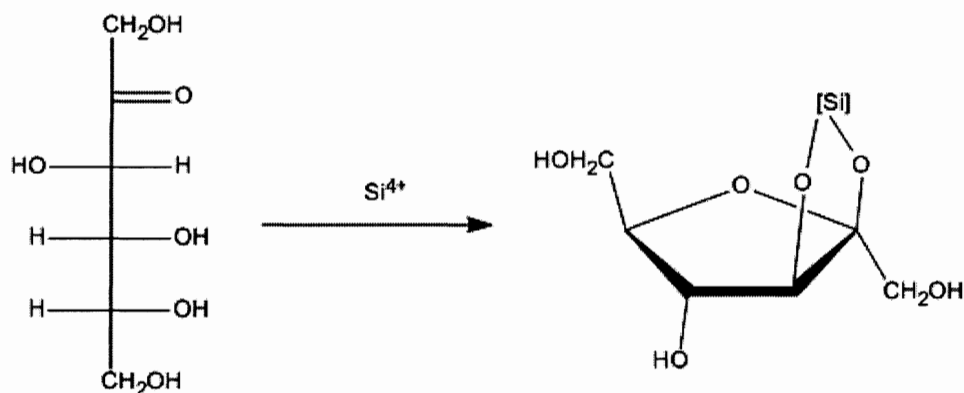
In this regard we have investigated the medical effects of chemical extractors specific to calcium and silicon on our synthetic samples. The two molecules chosen in this study to complex with calcium are nitrilo-*tris*-(methylene)phosphonic acid ( $H_6ntmp$ ) and citric acid. Fructose (open-chain and ring structures, **III**) is the most common sugar with the highest *cis* formation, and therefore it was chosen as our starting lead candidate for silicon chelation (Scheme 1.1). Vertical scanning interferometry (VSI) was used to monitor surface reactivity, topographical changes and the evolution of surface composition in real time with the aim of validating the ability of our complexing agents to form ligands or dissolve calcium and silicon. The ability of  $H_6ntmp$  to bind to calcium was further confirmed and quantified using  $^{31}P$  NMR analysis. IR analysis was conducted in order to adduce that calcium is indeed binding to citric acid.



(III)

### Result and Discussion

In the effort to determine the most accurate model for CBK growth, experiments were developed to test the factors that aid the formation of CBK type material. Multiple samples were synthesized mimicking the formation of the CBK material based on experimental analysis of the biological CBK material. Trends were noted based upon three factors: the presence of silicon, calcium and a lipid layer. Initial instrumental analyses on the human CBK samples were conducted for comparison to the synthetic material.



**Scheme 1.1.** Silicon-monosaccharide complex structure.<sup>9</sup>

**Analysis of human eye samples.** In order to determine a synthesis approach for the proposed synthetic material the elemental composition of human CBK samples obtained from two patients (**P1** and **P2**) was determined by XPS. The XPS data for the eye samples from different patients show the presence of calcium, carbon, oxygen, and silicon.<sup>7</sup> The quantitative elemental concentration results for the eye samples obtained from high resolution XPS analysis are reported in Table 1.1. The Si:Ca ratio ranges from 2.0 to 4.3 between samples, but is constant across each individual sample, suggesting that the composition is dependent on the patient. The elemental analysis of the samples obtained from human patients is interesting in two regards. First, the lack of detectable quantities of phosphorous in the XPS (< 0.1%) suggests that the role of phosphorous may be less important in CBK growth as previously have been suggested.<sup>10,11</sup> Second, the presence of silicon and the correlation of morphology with the silicon:calcium ratio suggest that silicon compounds may be important in the formation of CBK deposits. It must be noted that the presence of nitrogen in one of the patient's samples may suggest that the identity of biologically sourced organic matter has an effect on the composition and form of the precipitate.

**Table 1.1.** Summary of XPS data for eye samples and selected synthetic samples.

Sample	C (%)	O (%)	Si (%)	Ca (%)	N (%)
<b>P1</b>	65.1	21.7	3.4	1.7	7.0
<b>P2</b>	76.0	19.1	3.9	0.9	0.0
<b>3</b>	65.8	25.5	0.9	2.7	0.0
<b>6</b>	64.8	27.6	3.3	4.2	0.0
<b>10</b>	72.8	24.0	0.1	3.1	0.0
<b>20</b>	60.9	30.8	5.5	2.7	0.0

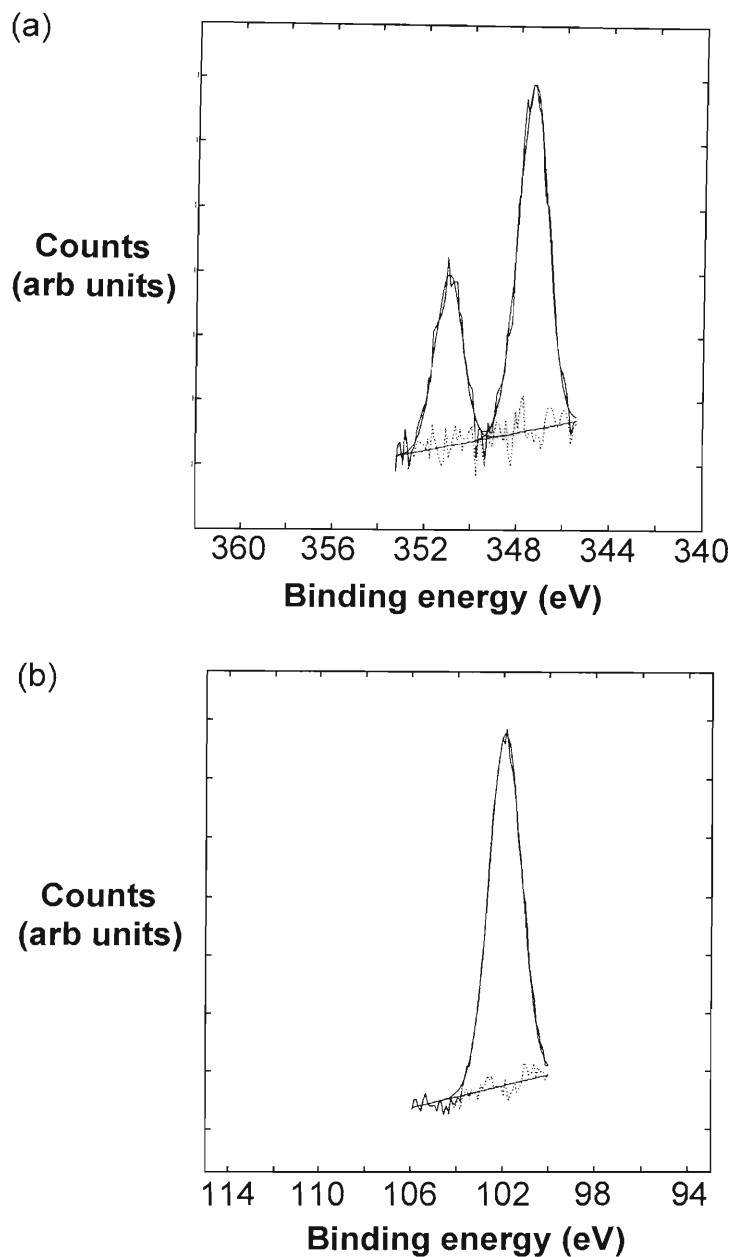


**Figure 1.3.** High-resolution (a) Ca2p<sub>3/2</sub> and (b) Si2p XP spectra for eye sample **P2**.

Peak fitting of the high-resolution Ca (2p<sub>3/2</sub>) and Si (2p) XP spectra indicated the presence of calcium carbonate and silicates, respectively (Figure 1.3). Based upon the Ca (2p<sub>3/2</sub>) spectra, it would appear that the calcium peak in the human sample **P2** can be

interpreted as being between that observed for the two polymorphs: calcite and vaterite.<sup>12</sup> Although the values for the synthetic materials are intermediate, they appear to be closer to those of vaterite. While vaterite is a metastable phase it does occur naturally in mineral springs, organic tissue, gallstones, and urinary calculi. The human samples were handled in non-silicone materials and were washed with DI water and MeOH prior to analysis to ensure that the silicon was not a surface contaminant due to handling. Furthermore, argon ion sputtering of the surface does not alter the Ca:Si ratio significantly. This indicates that the silicon is not a surface contaminant, but part of the bulk composition. This is confirmed in part by the Raman spectra of the eye samples (Figure 1.4) that indicate the presence of silicates (375, 392, 820, and 845  $\text{cm}^{-1}$ ) in general and a band at 1750  $\text{cm}^{-1}$ , which is indicative of  $\text{CaSiO}_3$ .

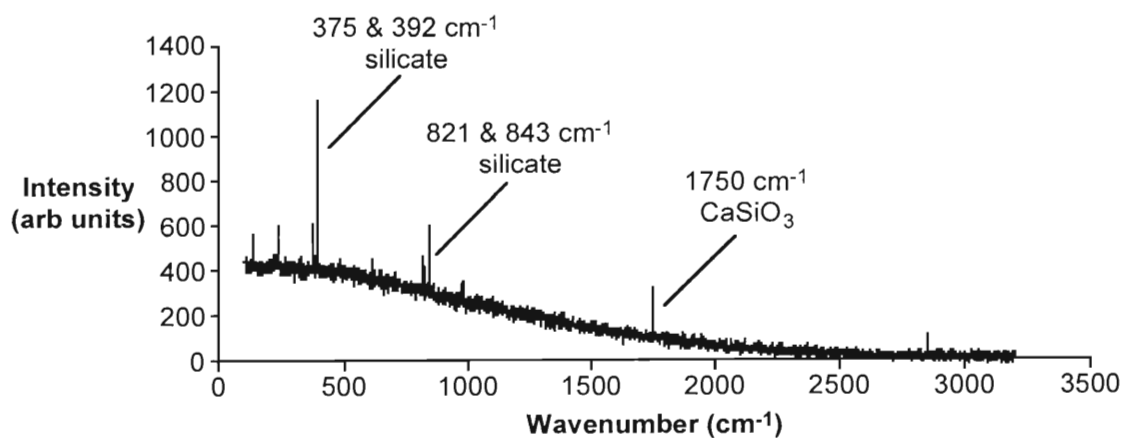


**Figure 1.4.** Raman spectrum of human eye sample **P1** showing peaks associated with various silicates.

SEM images of the eye samples show that the topography of the human eye sample contains small agglomerates resembling fused spherical shapes (Figure 1.5) within a matrix whose size ranges from 1 - 3  $\mu\text{m}$  in diameter. The size of the spheres is

related to the Si:Ca content of the samples. In eye sample **P1** where this ratio is 2:1, the spheres are smaller than the spheres in eye sample **P2** where the ratio is more than doubled (Table 1.2).

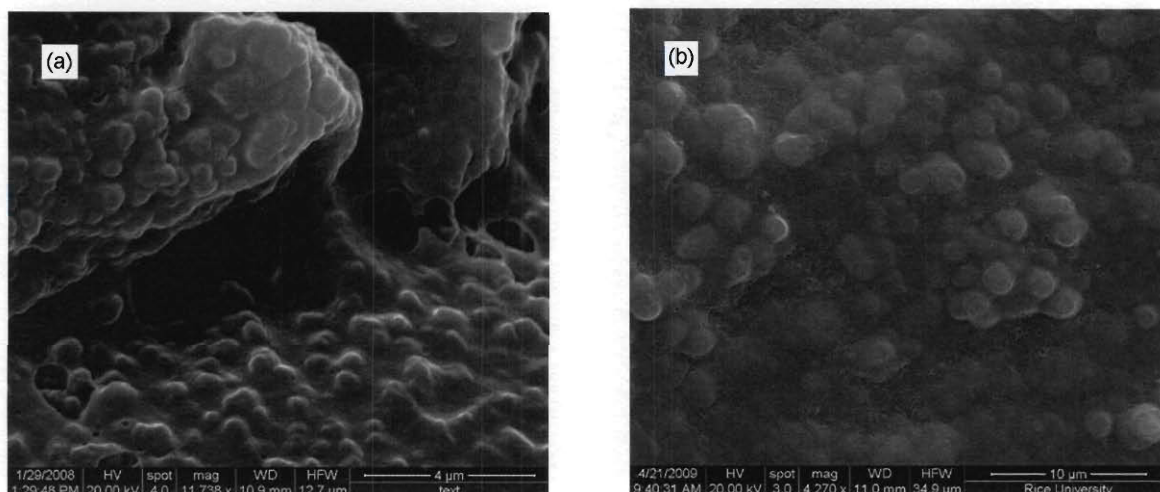


**Figure 1.5.** SEM image of eye samples **P1** (a) and **P2** (b) revealing small fused spherical shapes  $\sim 1 - 3 \mu\text{m}$  in size. The samples were taken from human patients at Baylor College of Medicine.

Based upon Raman spectroscopy as well as the presence of silicon in the XPS (even after sputtering) we suggest that silicon is an important component (and possible co-causative) of CBK.<sup>7</sup> Silicon as a nidus for calcium deposition is seen within the body during bone calcification. Silicon levels decrease drastically approaching maturity suggesting silicon is important in bone growth and mineralization of calcium within the bones.<sup>13</sup> Silicates are also important in the hydration of calcium silicate minerals to form hydrated silicates in cement.<sup>14</sup> Since silicon is known to act as a nidus for calcium growth, its presence in the human samples is consistent with its function as a nucleation site. The fusing of the spheres indicates that overgrowths of spheres were occurring. The large

percentage of carbon in the sample is due to lipids found on the outer layers of the eyes from tears and pores around the eyelid.<sup>15</sup> Based upon the appearance of fused spheres that are similar to the silica spheres obtained in the presence of surfactants,<sup>16</sup> we can suggest that the spheres in the human samples are a result of the surfactant (i.e., lipid material) acting as a template of silica/silicate growth. We have proposed, therefore, that excess silicon could also be a causative factor in CBK and silicon chelation therapy could play a role in treatment and prevention of the condition.<sup>7</sup> One issue to note is that the Si:Ca ratio appears to have significant latitude while maintaining the general morphology observed.

**Table 1.2.** The Si:Ca ratios as determined by XPS and sphere sizes as determined by SEM of selected samples.

Sample	Si:Ca from XPS	Sphere size ( $\mu\text{m}$ )
<b>H1</b>	2	1-2
<b>H2</b>	4.3	1-3
<b>3</b>	0.3	0.1
<b>20</b>	2.03	3

**Independent effects of surfactant and silicon.** In order to mimic the composition of the eye sample, various molar ratios of reagents were assessed. Table 1.3 summarizes the reaction conditions of each sample. With regard to the calcium source, we note that while our studies used pre-formed calcium carbonate, in the eye this probably results from the reaction of calcium salts with carbon dioxide, either from the atmosphere or dissolved.

**Table 1.3.** Summary of reaction conditions for the formation of CBK model materials in the absence of hydrocarbon.<sup>a</sup>

Sample	CaCO <sub>3</sub> (mg)	Fumed silica (mg)	Silicic acid (mg)	Silicone oil (mL)	SDS (mg)	TDPA (mg)	Time (h)
1	200	—	—	—	20	—	4
2	200	20	—	—	—	—	4
3	200	20	—	—	20	—	4
4	200	80	—	—	60	—	4
5	200	160	—	—	60	—	4
6	200	10	—	—	60	—	4
7	100	—	60	—	20	—	4
8	100	—	30	—	20	—	4
9	100	—	15	—	20	—	4
10	200	—	—	0.5	60	—	4
11	150	20	—	—	300	—	4
12	150	20	—	—	—	150	4
13	100	—	—	2	—	20	4
21	200	20	—	—	20	—	24

<sup>a</sup> SDS = sodium dodecyl sulfate; TDPA = tetradecylphosphonic acid.

In the first set of experiments the effect of a surfactant (SDS, IV) alone on the calcium carbonate solution was tested (synthetic sample 1). Although SDS is not present



in the body, it was chosen to simulate the lipids that would be present in the pre-ocular tear film and ocular tissues,<sup>15</sup> and because we have previously observed its ability to seed spherical particles of silica.<sup>16</sup> The SEM image of this sample showed the formation of calcium carbonate sheet like structures as shown in Figure 1.6a. The sheet-like morphology is typical for calcium carbonate precipitation in the absence of a template.<sup>17</sup> Elemental analysis performed by XPS, Raman and XRD all confirmed the presence of  $\text{CaCO}_3$  crystals. It is clear, therefore, that a surfactant-like chemical is insufficient to form calcium spheres and that the presence of silicon is important in creating the CBK-type of material.

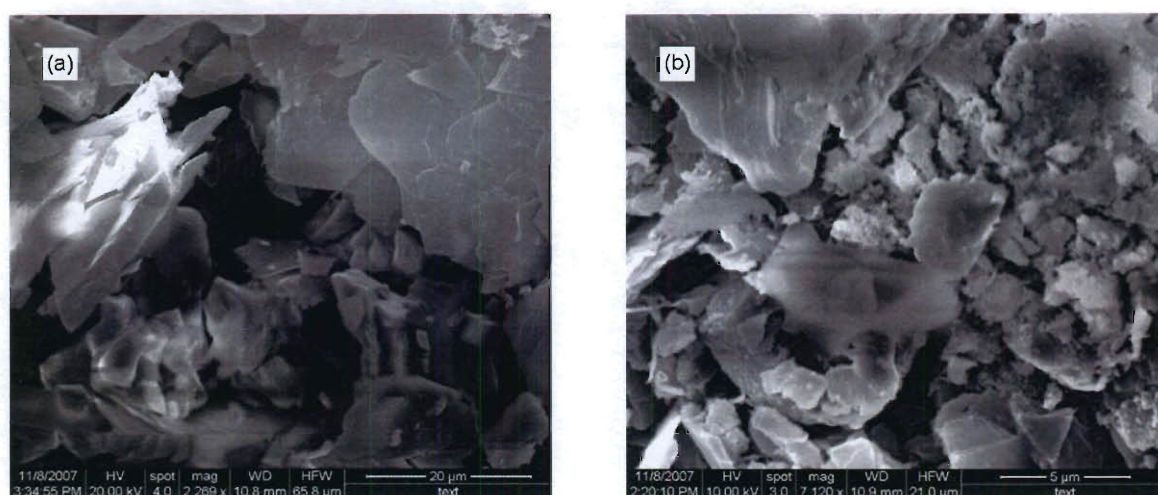
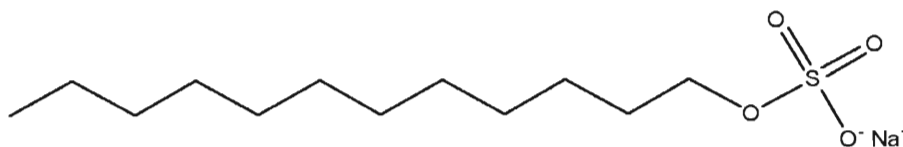


**Figure 1.6.** SEM images of calcium silicate grown in the presence of (a) SDS (sample 1) and (b) fumed silica (sample 2) showing the presence of typical crystallites of  $\text{CaCO}_3$ .

The effect of silicon (fumed silica) on the  $\text{CaCO}_3$  precipitation in the absence of a surfactant was also studied (Table 1.3, sample 2). This sample developed jagged sheets (Figure 1.6b) that resembled the appearance of sample 1. The Raman and XRD analysis of this sample mainly showed calcium carbonate in the final product. Again, the

formation of a CBK-like deposit is not simply a function of the presence of calcium and silicon.



(IV)

**Combined effects of surfactant and silicon.** The influence of silicon in the formation of CBK when added to a calcium carbonate solution in the presence of SDS was examined in sample **3** (Table 1.3). In the presence of silicon, the morphology of the structures changed from sheets to spheres (Figure 1.7), having a closer resemblance to the biological sample (*c.f.*, Figure 1.5). The spherical shapes are smaller in size (100 nm) than observed in samples **P1** and **P2**; however, the size appears to be broadly dependant on the Si:Ca ratio (Figure 1.8), suggesting that the spheres are silicon rich.

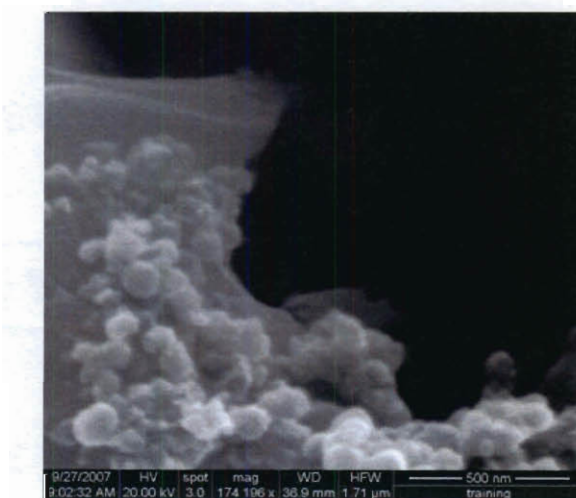


**Figure 1.7.** SEM image of sample **3** showing fused spherical features in a matrix.

XPS data showed that this sample was composed of carbon, oxygen, silicon, and calcium (Table 1.1). The elemental percentages of carbon and oxygen in this sample closely resembled the ones observed in the human eye samples, however, this sample is much more calcium rich in compare to the eye samples having a Si:Ca of 0.3:1. As observed with the two eye samples, the increased calcium content results in smaller sphere sizes. Therefore, the small sphere sizes observed in sample 3 are believed to be due to its high calcium content. Curve fitting of the Ca and Si regions of sample 3 obtained from high resolution XPS indicated the presence of calcium carbonate and silicates, respectively (Table 1.4), which match the data from the human samples; however, the Raman spectra of sample showed the presence of both calcium carbonate and silica, but not specific silicate phases. This latter observation suggests that biological mineralization is more prevalent than chemical crystallization.

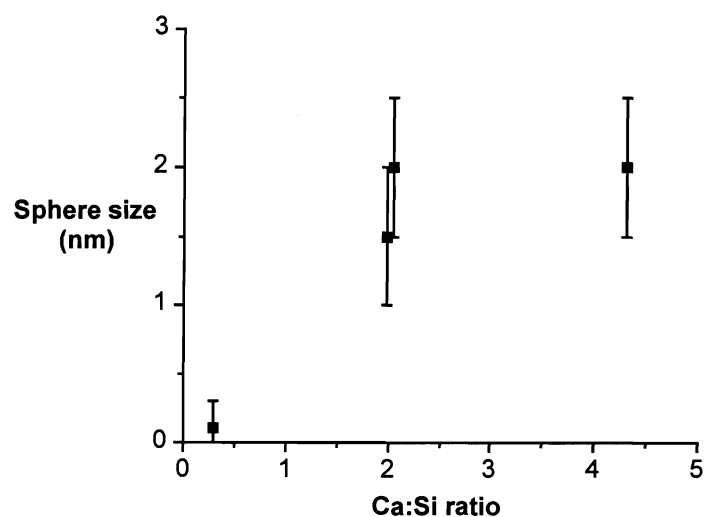


**Figure 1.8.** Plot of sphere size as a function of Si:Ca ratio for eye samples **P1** and **P2** in comparison with synthetic samples **3** and **20**.

While the synthetic samples can mimic the composition and morphology of the human eye samples, the crystallinity and crystal phases were not the same. In an effort to see if this is a function of crystal growth, sample **3** was thermally annealed at 500 °C (for 2 and 4 hours) and then at 700 °C (again for 2 and 4 hours). The Raman spectrum and XRD were collected after each stage. Raman spectra of annealed samples at both temperatures revealed a dramatic decrease in their signals of crystalline  $\text{CaCO}_3$  and showed no signals indicative of silica in compare to sample **3**. The low signal intensity for  $\text{CaCO}_3$  may be due to decomposition of the sample into CaO at these temperatures although no CaO was detected. These results are supported by the XRD data. Data derived from the X-ray patterns of the annealed samples demonstrated the presence of a predominant calcium carbonate phase (calcite), similar to XRD patterns of sample **3**; however, intensity of these lines was much weaker. Additionally, no diffraction lines related to silica or silicate appeared in the XRD patterns of the annealed samples. In biological systems, crystal growth is greatly influenced by local factors present in the system such as surfactant like lipids and other organic molecules, neutral pH, temperature, and presence of ions.<sup>18</sup> Although care was taken to mimic the biological environment closely, due to the complexity of the biological systems it was merely impossible to emulate the same settings for our artificially crystal growth systems. Additionally, in contrast to synthetic samples that are prepared in a short period of time, mineralization processes including CBK calcification usually progress very slowly. Given the inevitable differences among the synthetic and biological samples reaction conditions and times, above observed disparity in Raman data is not unreasonable.

Our findings strongly suggest a correlation between the presence of silicon and the formation of CBK. In addition, the lack of surfactant in sample **2** which resulted in production of non-spherical shapes confirms the need for a lipid (or lipid-like additive). In agreement with our previous studies,<sup>14</sup> it seems SDS aids sphere formation by possibly

making micelles, which act as a template for silicon deposition and ultimately Ca-Si fused complex formation.<sup>19</sup> As a result, it appears the interaction of the silicon and calcium with biological lipids is a major factor in the development of CBK. This system was proposed as our initial CBK model material.

**Table 1.4.** Selected binding energies obtained from high resolution XPS data.

Sample	Binding Energy (eV)	
	Si2p	Ca 2p <sub>3/2</sub>
<b>H2</b>	102.02	346.91
<b>3</b>	102.52	347.37
<b>20</b>	103.08	347.27
SiO <sub>2</sub>	103.1-103.8	—
Silicates	102.0-102.9	—
CaCO <sub>3</sub>	—	346.5 – 347.9

**Effect of silicon concentration and source.** The effects of various silicon and surfactant sources and reaction time on the precipitate's morphology were investigated. The concentration of fumed silica was varied (in comparison to our initial CBK model material) in order to determine effect of the silicon concentration on the sphere size. When the amount of fumed silica was increased by four and eight fold (samples **4** and **5**,

respectively, see Table 1.3) the SEM images showed formation of very small semi-spherical shape (100 nm) crystals (Figure 1.9a).

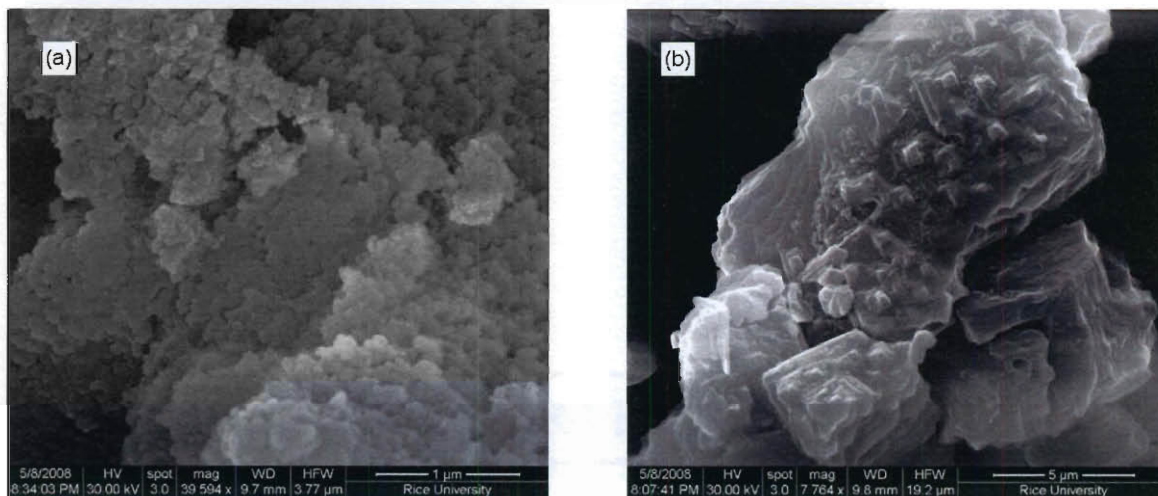


**Figure 1.9.** SEM images of samples prepared with (a) 4x the silica (sample **4**) and (b)  $1/2$ x the silica (sample **6**) as compared to sample **3** (see Figure 1. 6).

Raman and XRD data confirmed the presence of calcium carbonate and silicon in the products. The increase in the amount of silica does not seem to affect the morphology of the structure but the size and chemical composition of the material does not match with ones found in either of the human eye samples (**P1** and **P2**). Lowering the amount of fumed silica (as compared to sample **3**) produced crystals (sample **6**) with similar chemical composition to the eye samples; however, the SEM image (Figure 1.9b) showed development of large cubic aggregates  $>5 \mu\text{m}$  in size.

While the choice of fumed silica as a silicon source was chosen based upon our prior research,<sup>16,20,21</sup> it is important to determine if any form of silicon could initiate the formation of CBK-like material. To test this theory, silicic acid was selected as an alternative silicon source. Silicic acid is the form of silicon predominantly absorbed by

humans and is found in numerous tissues including bones, tendons, aorta, liver, and kidney.<sup>22</sup> Reactions performed with various concentration of silicic acid as the silicon source all failed to create a product which resembled the eye sample (samples 7 - 9). SEM images of these samples (e.g., Figure 1.10) showed sheet like structures.

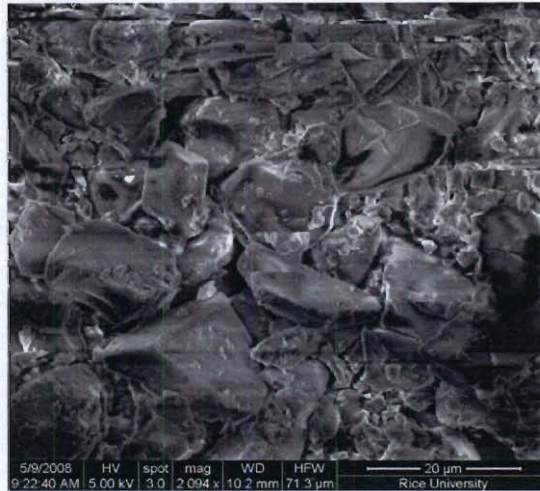


**Figure 1.10.** SEM image of sample 7 formed using silicic acid.

Silicone oil has been associated with the formation of CBK in the eyes of many patients when administered to cure retinal tears, and other surgeries, including: proliferative vitreoretinopathy proliferative diabetic retinopathy, and other retinal detachments (RDs).<sup>23</sup> Silicone oil is injected into the eye, to replace the vitreous gel, at the time of surgery for the repair of retinal detachments. Several long-term studies have shown that calcific band keratopathy can occur in up to 16% of aphakic eyes after silicone oil injection and in up to 100% of eyes with silicone oil/endothelial touch.<sup>23,24</sup> Further evidence for the effects of silicon on ocular calcification came from the experience of hydrogel intraocular lenses (IOL) which were packaged in a silicon-gasket packaging system known as the Surefold<sup>®</sup> system. Patients developed calcium deposits

on these IOLs within 29 months of implantation.<sup>25,26,27</sup> Therefore, silicone oil was chosen as an alternative source of silicon for this study. Sample obtained from this reaction (sample **10**) showed formation of fused semi-spherical shapes of *ca.* 5  $\mu\text{m}$  (Figure 1.11) relatively more similar to the shape and morphology of the fused spheres observed in the eye samples in comparison to our preceding synthetic samples. When compared to the results of the human eye samples, the XPS data of sample **10** showed similar quantity of carbon and oxygen, however, the calcium content is much higher and the amount of silicon is significantly lower as listed in Table 1.1. The Raman and XRD both revealed the presence of  $\text{CaCO}_3$  and silicon in the final product.

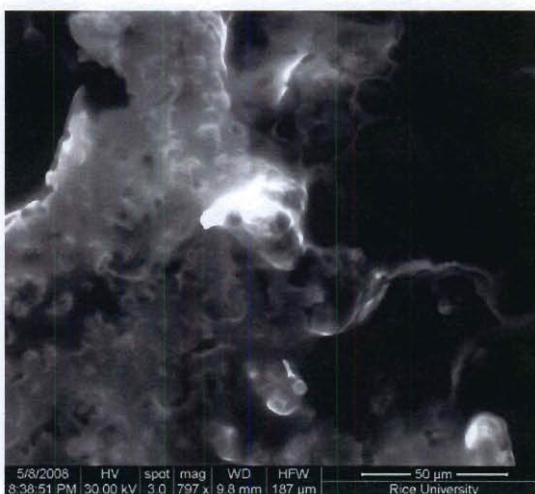
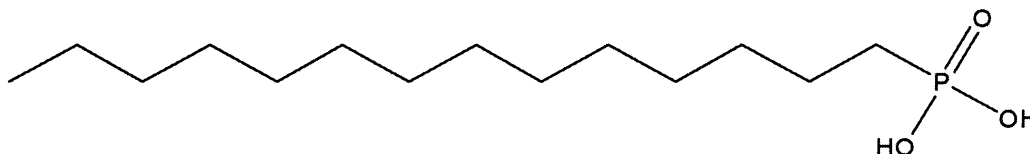


**Figure 1.11.** SEM images of sample **10** formed using silicone oil as the silicon source.

**Effect of surfactant concentration and source.** With the aim of mimicking CBK material more precisely, the outcomes of varying amounts and type of surfactant on the selected CBK model material were examined next. Notwithstanding we did not observe significant quantities of phosphorous in either of the eye samples, it has been reported that phosphonate salts are sometimes found in CBK samples.<sup>10,11</sup> Therefore, a



phosphonic-capped surfactant was chosen, tetradecyl phosphonic acid (TDPA, **V**), as the alternative surfactant source, which is a biological lipid signaling molecule.



(**V**)

Increased amount of SDS in the reaction (Table 1.3, sample **11**) caused formation of fused cubic structure with characteristic peaks of calcium carbonate observed in both Raman and XRD spectra. When SDS was replaced with TDPA (sample **12**), in presence of fumed silica as the silicon source, a sheet like structure was formed. This sample showed characteristic peaks of  $\text{CaCO}_3$  in Raman and formation of Ca-Si bond in XRD.

When silicone oil and TDPA were used as the sources of silicon and surfactant, respectively (sample **13**), the final product showed formation of fused semi-spherical shapes (Figure 1.12) comparable to the shape and morphology of the spheres observed in the eye samples but much larger in size *ca.* 10 - 25  $\mu\text{m}$ . This morphology was also seen in our previous sample (sample **10**) that was prepared with silicone oil. These results not only indicate that silicone oil might be a good silicon source for formation of synthetic CBK, it also further confirms the role of silicon in formation of biological CBK.

**Effect of hydrocarbon.** The presence of non-polar compounds that are present in the human eye, were also tested to determine their influence on formation of CBK materials. Hexane was chosen as a model aliphatic compound to examine the effect of a non-polar hydrocarbon with our model system. Although, hexane is not present in the eye,

it is a simple non-polar hydrocarbon, which is readily available and would certainly provide insight into changes associated with the presence of non-polar species. On the other hand, the non-polar compounds that compromise the eye typically have higher carbon ratios; therefore, dodecane was also used in our system separately to study the possible effect of using a longer carbon chain (Table 1.5).

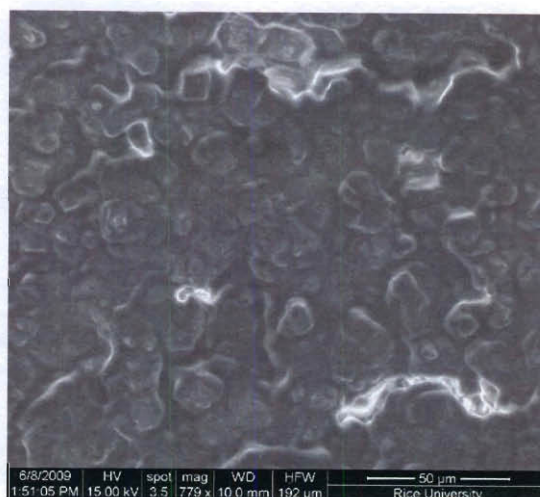


**Figure 1.12.** SEM images of sample **13** .

The growth of  $\text{CaCO}_3$  crystals in the presence of hexane and surfactant (SDS) showed development of large sheets and small particulate shapes ( $<100$  nm) (sample **14**). These shapes (Figure 1.13a) do not resemble those seen in the eye sample (Figure 1.5). It is our belief that hydrocarbons act as a template for  $\text{CaCO}_3$  crystal growth here. On the other hand, when the growth was performed in presence of hexane and silicone (fumed silica) alone, a cubic morphology was observed as seen in Figure 1.13b (sample **15**). This reaction failed to make spherical shapes as seen in the eye sample that is consistent with the theory that the surfactant lipid layer acts as a template for calcium-silica formation.

**Table 1.5.** Summary of reaction conditions for the formation of CBK model materials in the presence of hydrocarbon.<sup>a</sup>

Sample	CaCO <sub>3</sub> (mg)	Fumed silica (mg)	Silicic acid (mg)	Silicone oil (mL)	SDS (mL)	TDPA (mg)	Hexane (mL)	Dodecane (mL)	Time (h)
<b>14</b>	200	0	—	—	20	—	20	—	4
<b>15</b>	200	20	—	—	—	—	20	—	4
<b>16</b>	200	20	—	—	20	—	20	—	4
<b>17</b>	200	20	—	—	20	—	—	20	4
<b>18</b>	200	—	200	—	20	—	20	—	4
<b>19</b>	200	—	20	—	—	10	20	—	4
<b>20</b>	100	—	—	1	—	15	20	—	4
<b>22</b>	200	20	—	—	20	—	20	—	24

<sup>a</sup>SDS = sodium dodecyl sulfate; TDPA = tetradecylphosphonic acid.

The reaction of calcium carbonate, fumed silica and SDS in presence of hexane formed spherical shapes about 50 nm in diameter (sample **16**); however, these spheres were not fused in a matrix as observed in the biological samples. All instrumental analysis including XRD, XPS and Raman confirmed the presence of both silicon and calcium carbonate. Similarly, this reaction in presence of dodecane as the hydrocarbon source produced spherical shapes about 10 nm in diameter (sample **17**). It seems the addition of hydrocarbon to our initial CBK model material induces the formation of

smaller spheres and using the longer hydrocarbon chain has little to no effect on the system. Figure 1.14 demonstrates the SEM images of these two samples.

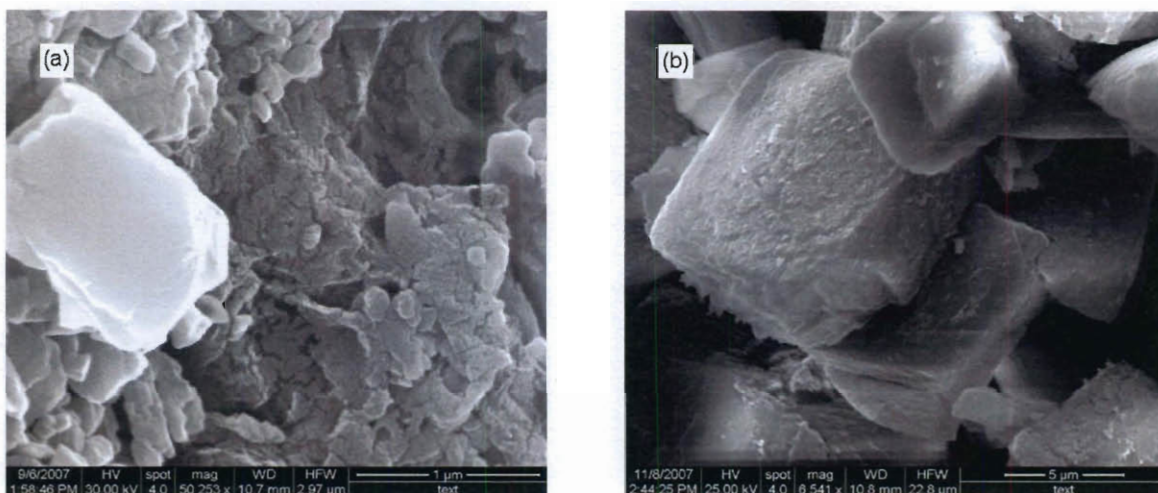


**Figure 1.13.** SEM images of (a) sample 14 and (b) sample 15 showing the effect of adding a non-polar compounds (hexane) to the calcium/silica reaction

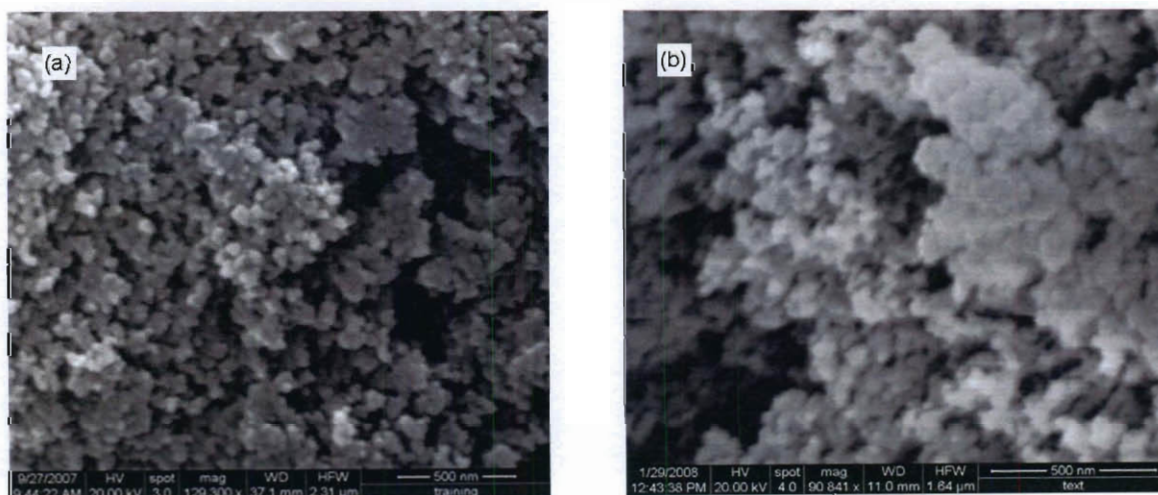


**Figure 1.14.** SEM images of (a) sample 16, and (b) sample 17 showing the formation of very small non-fused spheres with the addition of hexane and dodecane, respectively.

When the silicon source was changed to silicic acid, the SEM image of the final product showed sheets of material about *ca.* 5  $\mu\text{m}$  in size (sample **18**). This result is similar to our earlier results where silicic acid was used as the silicon source in absence of hydrocarbon. However, silicic acid in presence of TDPA as the surfactant source (sample **19**) formed semi-spherical  $\text{CaCO}_3$  crystal *ca.* 5 - 10  $\mu\text{m}$  in size (Figure 1.15).

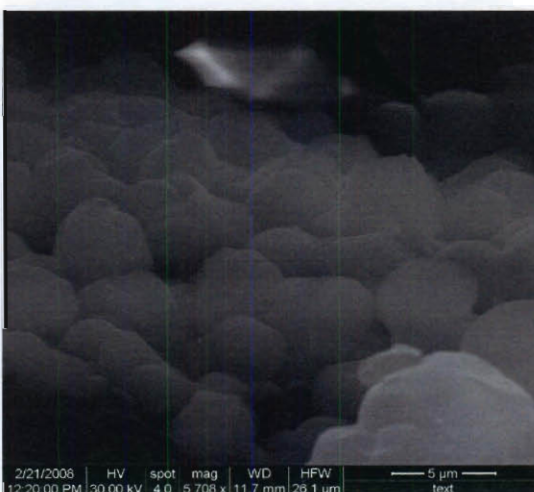


**Figure 1.15.** SEM image of sample **19**.

Finally, the reaction of silicone oil and TDPA, as the respective sources of silicon and surfactant, with calcium carbonate in the presence of hexane was investigated. The SEM image of this sample (sample **20**) showed fused spherical shapes that are very similar to the shape and morphology of the human eye samples as shown in Figure 1.16. According to the XPS data, the Ca:Si ratio of this sample is the nearest to the Ca:Si of the human eye samples, more specifically to eye sample **P1** (Table 1.2). Although, the Raman spectrum of this sample is rather complex due to the addition of the siloxane to the system (Figure 1.17), the XRD and high resolution XPS both show the presence of calcium carbonate and silicon in the final product.

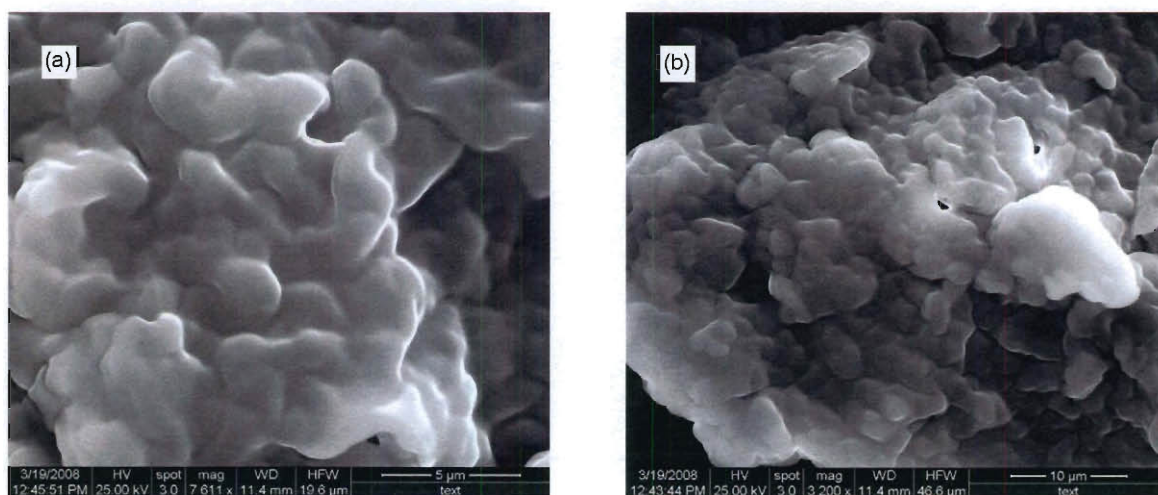


**Figure 1.16.** SEM images of sample **20** showing the formation of highly fused spheres.

The high-resolution Ca ( $2p_{3/2}$ ) and Si (2p) peaks for sample **20** (Figure 1.18) are at 347.27 eV and 103.08 eV, respectively, which can be compared to those of pure  $\text{CaCO}_3$  (346.6 eV) and  $\text{SiO}_2$  (103.3 eV). The similarity suggests the presence of similar chemical identity (Table 1.4). In comparison to all our other synthetic samples, sample **20** has one of the closest resemblances to the human eye samples with regard to morphology, sphere size, and chemical composition.

**Effect of reaction time.** Samples **3** developed the spherical morphology as seen in the original eye samples (**P1** and **P2**) but the size of the spheres was smaller than the ones seen in the eye samples. Although the size of the fused spheres is clearly dependant on the Si:Ca ratio, it is also possibly a function of the slower *in-vivo* reaction rates. Thus, in an effort to control the size of the spheres, we experimented with the reaction time. The chemicals used in sample **3** were reacted over 24 hours to test if the spheres found in the SEM image of sample **3** would increase in size. According to SEM extended reaction times (sample **21**) failed to create spherical shapes. This reaction was then repeated in

presence of hexane for 24 hours (sample **22**) that also failed to create spherical shapes. Based on these two samples, we believe over time the calcium/silica spheres are forming large aggregates creating large sphere/cube like structures.

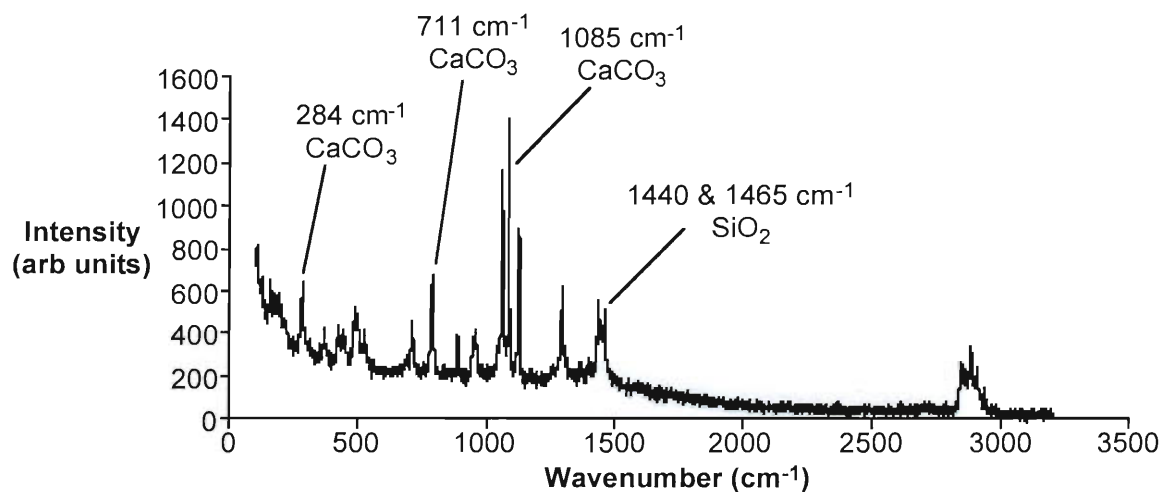


**Figure 1.17.** Raman spectra of sample **20**.

In the effort to determine the respond of our developed synthetic model system to the chosen chemical extractors we conducted a series of dissolution studies. We used calcium carbonate and fume silica as starting reference materials and sample **20** which had the closest resemblance to the human eye samples as our synthetic model material for these studies. We also monitored the reaction of sample **20** with all of our complexing agents in real time utilizing VSI. Additionally, we monitored and verified the complexation of H<sub>6</sub>ntmp with calcium carbonate and sample **20** using <sup>31</sup>P NMR. Reaction of citric acid with sample **20** was also confirmed with IR.

**Sample dissolution.** With the aim of dissolving the CBK material more efficiently, the outcomes of varying concentration and pH of solutions on the reference material were examined first. Both calcium carbonate and fume silica showed no

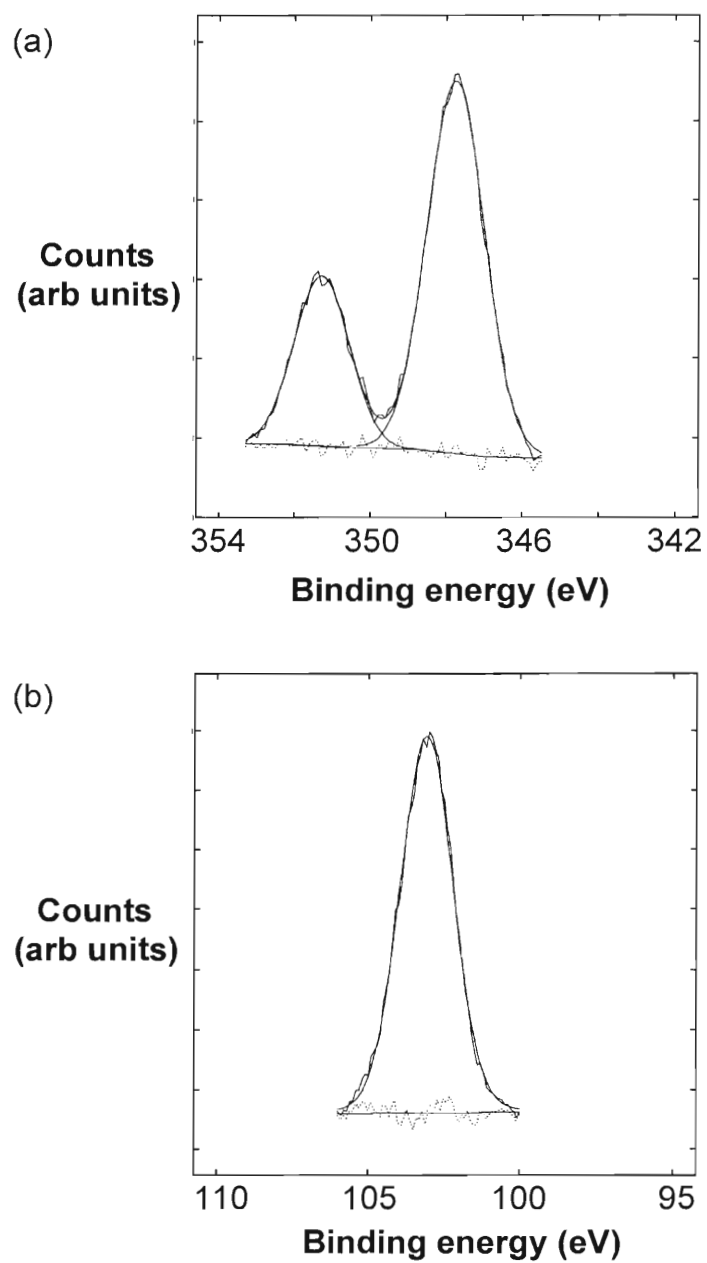


**Figure 1.18.** High-resolution XPS spectra of sample **20** (a) Ca<sub>2p<sub>3/2</sub></sub> and (b) Si<sub>2p</sub>.

significant dissolution in 1% solutions of H<sub>6</sub>ntmp, citric acid and fructose in DI water with adjusted pH of 7. Although CaCO<sub>3</sub> initially dissolved completely in 5% solutions of



H<sub>6</sub>ntmp and citric acid with adjusted pH of 7, the dissolution was slow and after 24 hour, precipitates were formed. When pH of H<sub>6</sub>ntmp solution was adjusted to 6.5, dissolution occurred slowly but no precipitate formation was observed after 24 hours. Calcium carbonate reacted spontaneously and completely with 5% citric acid solution of pH 6.5. Fume silica, on the other hand, showed no dissolution in a 1% or 5% fructose solution of pH 7, but when pH was adjusted to 6.5, complete dissolution occurred and no precipitate formed after 24 hrs. These results indicated that at the 5% solution concentration with pH of 6.5 not only dissolve the reference material but prevent precipitation of the ligands or complexes as well. This concentration and pH were chosen for further VSI, NMR and IR studies of sample **20**.

Sample **20** completely dissolved in 5% H<sub>6</sub>ntmp and citric acid solutions and no precipitate formed even after 24 hours. Dissolution of sample **20** in the 5% fructose solution was none or insignificant. This result is not surprising considering that this sample contains only about 5% silicon material.

**VSI experiments.** Sample **20** was reacted with 50 μm of H<sub>6</sub>ntmp solution for 15 min, 30 min, and 1 h. Figure 1.19 show the evolution of surface topography with reaction time. We can observe a distinguished reaction sequence: an initial surface etching followed by subsequent precipitation. This result is consistent with reaction steps reported by our group's previous study.<sup>3</sup> First, a rapid surface etching occurs which brings about an overall reduction in surface height of about 15 μm along with increase in surface area and roughness. Next is a slow growth phase in which the surface shows an increase in height of 5 μm. This stage is associated with the formation of a calcium phosphonate complex. Formation of the calcium phosphonate precipitates in eye should not be of any concern since the complex will be excreted out the eye via tears through the nasolacrimal duct soon after formation and before precipitation.

Due to earlier bench-top observation of the quick reaction of  $\text{CaCO}_3$  with citric acid solution, we decided to monitor reaction of sample **20** with this solution at 1 min intervals. After application of 50  $\mu\text{m}$  solvent, a large etch pit was formed within the first minute of reaction. The surface height change observed for this reaction was about 25  $\mu\text{m}$  and no significant change was observed after the initial pit formation (Figure 1.20). This observation not only confirms our former results that sample **20** completely dissolves in citric acid solution it also verifies that sample remains dissolved till removed from the surface. No surface change was observed following the first minute of reaction due to complete dissolution of the sample material in the solvent and its removal upon solvent aspiration.

Reaction of sample **20** with fructose solution was monitored for 15 min, 30min, 1 h and 3h and no surface topography change was observed (Figure 1.21). The overall surface height remained the same throughout the reaction. This result is comparable with our bench-top studies of sample **20**. Even though we had seen complete dissolution of fume silica in this solution no dissolution was observed for sample **20** during our bench-top studies. Silicon composition in sample **20** is infinitesimal in compare to fume silica, therefore, the result obtained from the VSI analysis seems reasonable and no further chelation studies of this solution was carried out.

**Spectroscopic studies.** Complexation of  $\text{H}_6\text{ntmp}$  with calcium carbonate was monitored by  $^{31}\text{P}$  NMR spectroscopy. Calcium carbonate was incrementally added to a solution of  $\text{H}_6\text{ntmp}/\text{D}_2\text{O}$  with adjusted pH of 6.5 over time and ligand formation was monitored against the 5%  $\text{H}_6\text{ntmp}/\text{D}_2\text{O}$  standard solution. The  $^{31}\text{P}$  NMR spectra of the standard solution showed a triplet at 8.2 ppm. Complexation of calcium to  $\text{H}_6\text{ntmp}$  was readily observed by  $^{31}\text{P}$  NMR (Figure 1.21). As more  $\text{CaCO}_3$  was added to the

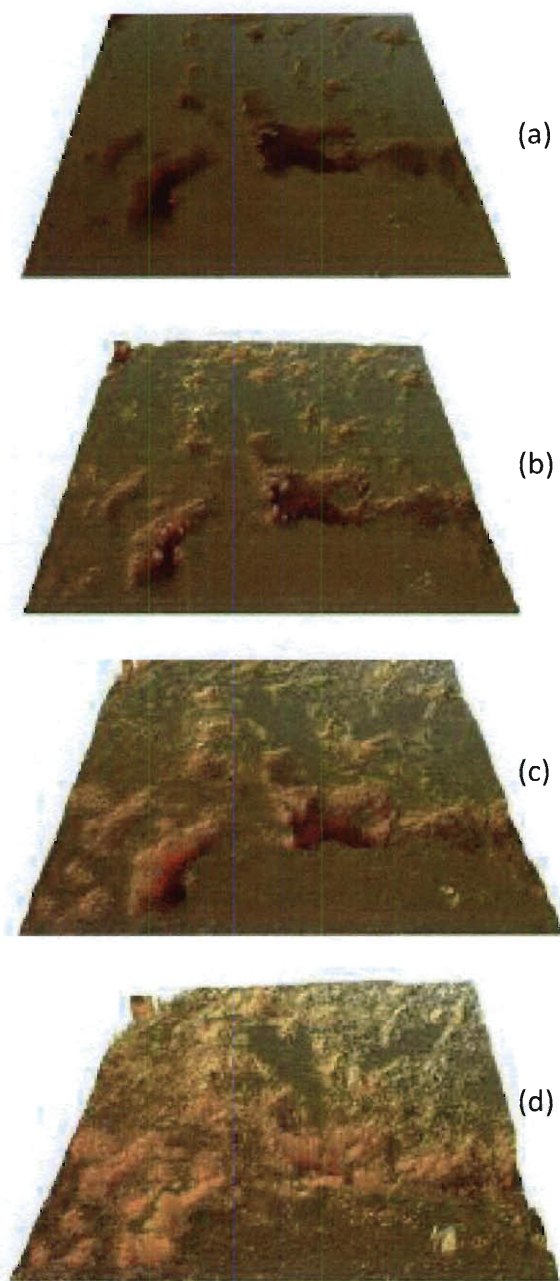


**Figure 1.19.** VSI maps of sample **20** surface (80x objective) showing the initial surface (a), and reaction sequence of this surface exposed to  $H_6ntmp$  solution at 15 min (b), 30 min (c), and 1 h (d).

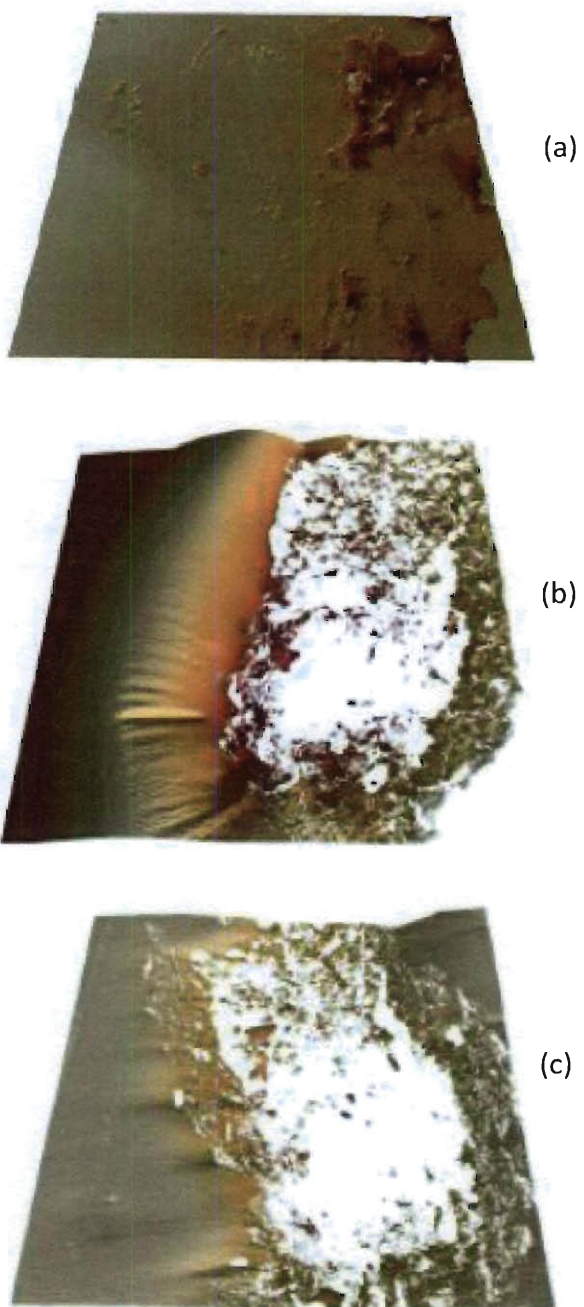


**Figure 1.20.** VSI maps of sample 20 surface (10x objective) of the initial surface (a) and reaction of this surface exposed to citric acid solution at 1 min while removing solvent (b), at 1 min. after solvent removal (c).

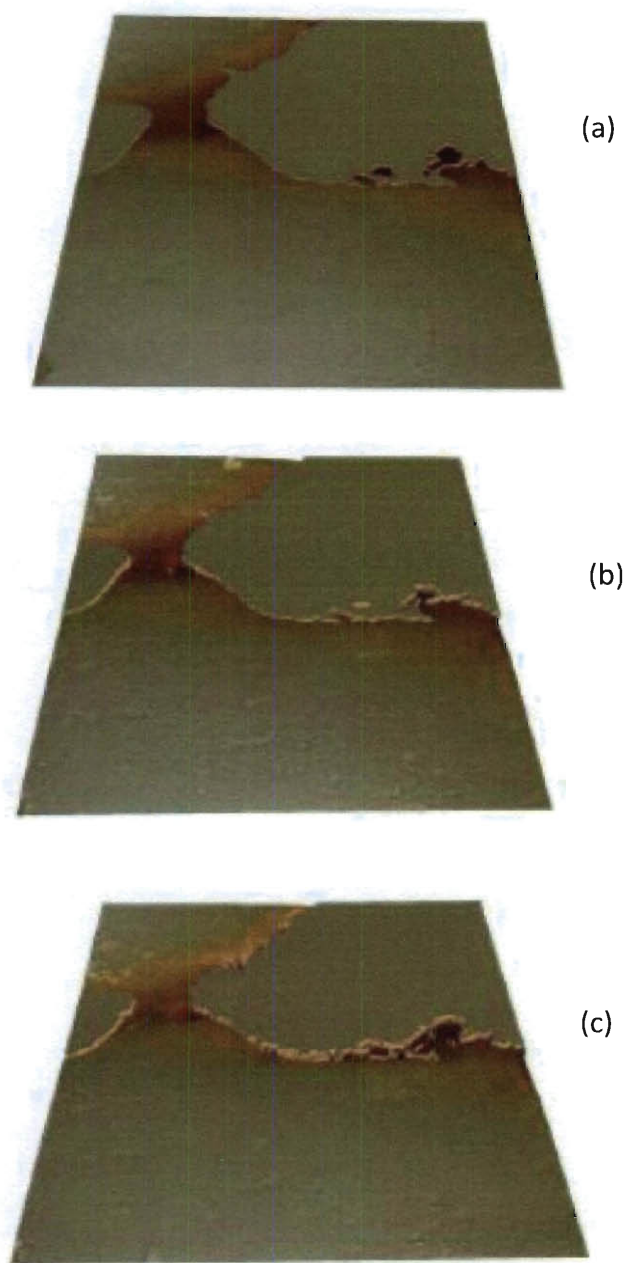


**Figure 1.21.** VSI maps of sample **20** surface (80x objective) of the initial surface (a), and reaction sequence of this surface exposed to fructose solution at 1 h (b), and 3 h (c).

$H_6ntmp/D_2O$  solution, the intensity of the triplet peak decreased, signifying the formation of the calcium phosphonate complex.

Complexation of  $H_6ntmp$  with sample **20** was also examined using the same procedure specified above. The  $^{31}P$  NMR spectra of this sample showed ligand formation patterns that are very similar to the ones observed with our reference  $CaCO_3$  material (Figure 1.22). This result is very encouraging and provides conformation that  $H_6ntmp$  ligand indeed binds well to our synthetic sample and could possibly be used as a therapy for human CBK samples as well.

To study the ability of citric acid to chelate with calcium IR studies were conducted to adduce that calcium is binding to citric acid. The C-O stretch for carbonyl ( $\sim 1710\text{ cm}^{-1}$ ) and C-O stretch ( $1200\text{ cm}^{-1}$ ) will shift to a lower frequency with the addition of calcium material.<sup>28</sup> In addition, the OH stretch will begin to disappear due to the chelation to the calcium. These changes in the IR signify the formation of the calcium-oxygen complex. The IR spectra of citric acid and citric acid and sample **20** mixture were collected dried from solvent. Figure 1.23, is an overlap of the original IR taken before sample **20** was added and after. As predicted there are shifts in the carbonyl and C-O stretch due to the addition of our calcium containing sample. It appears that sample is forming the Ca complex with the citric acid. This complex will not precipitate and will remain in solution till removed as our VSI experiment revealed earlier. Therefore, we believe that citric acid makes a promising therapeutic candidate for human CBK samples.

### Conclusions

In developing an *ex-situ* model for subsequent studies, we have shown that in order to mimic the morphology and composition of human samples, there are three components that are required: 1) a calcium source, 2) a silicon source, and 3) a surfactant

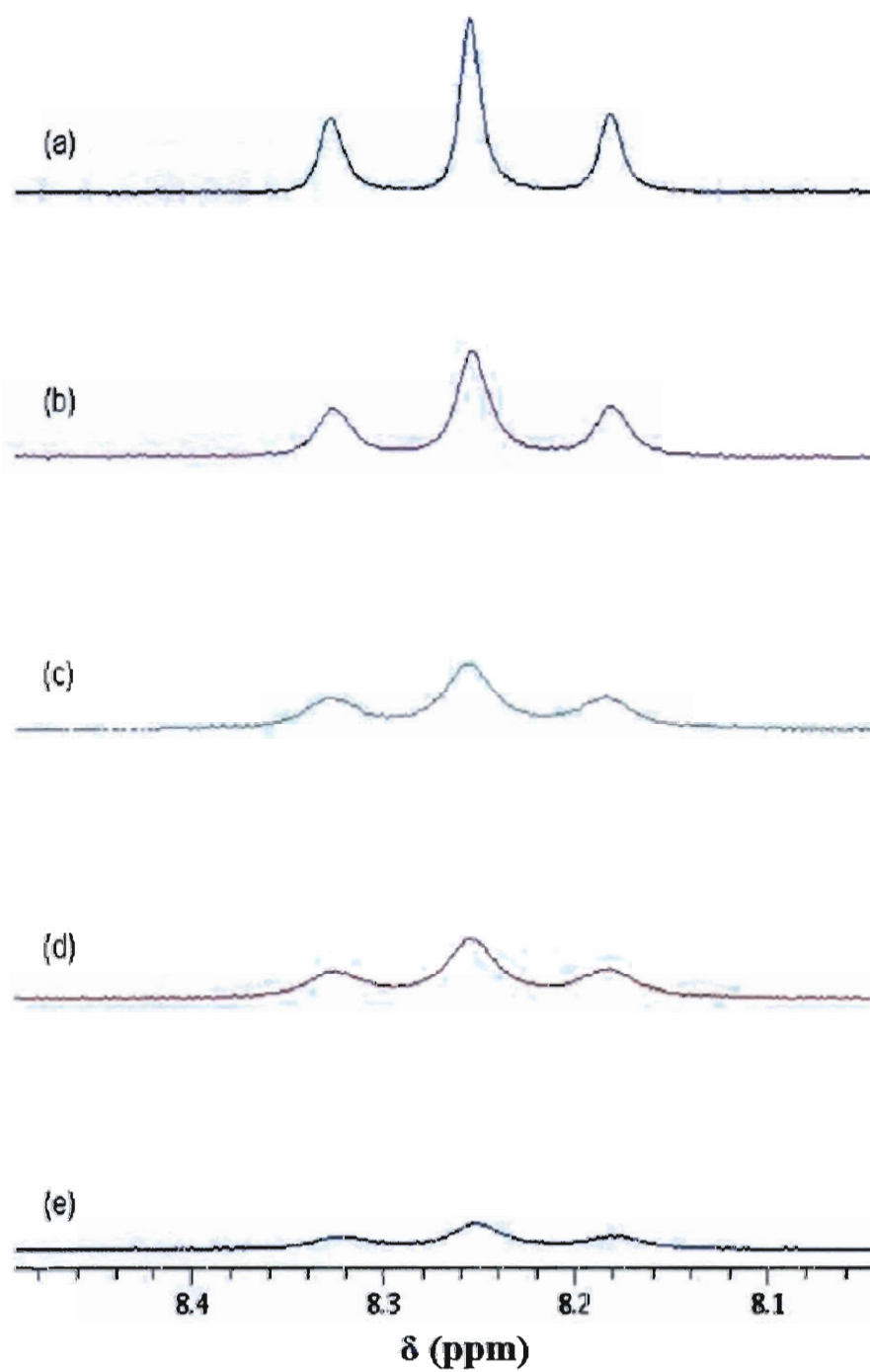


**Figure 1.22.**  $^{31}\text{P}$  NMR spectra of  $\text{H}_6\text{ntmp}$  solution (a) and its reactions with 2 mg (b), 6 mg (c), 10 mg (d), and 14 mg (e) of  $\text{CaCO}_3$ .

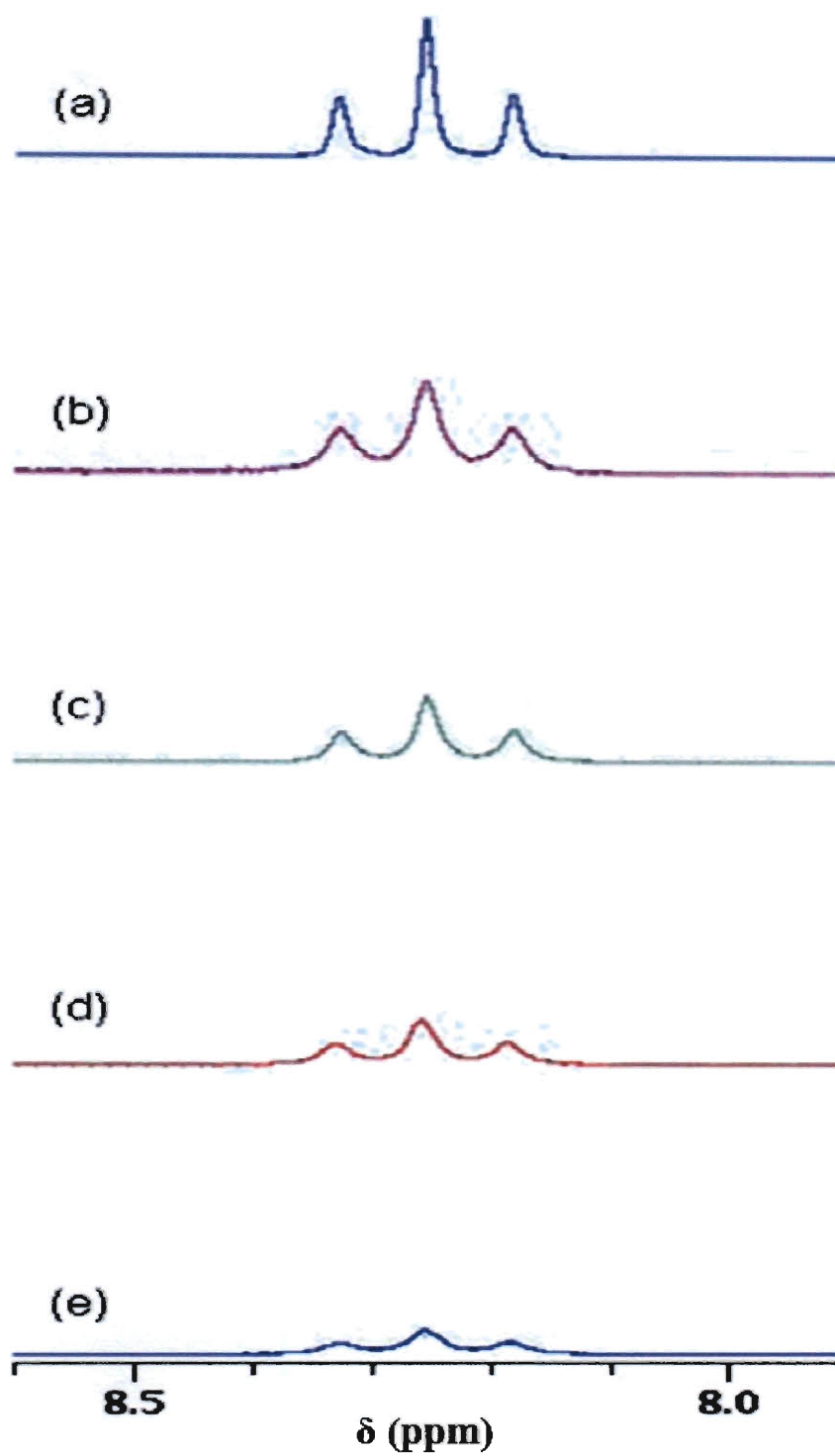


**Figure 1.23.**  $^{31}\text{P}$  NMR spectra of  $\text{H}_6\text{ntmp}$  solution (a) and its reactions with 2 mg (b), 4 mg (c), 8 mg (d), and 16 mg (e) of sample **20**.



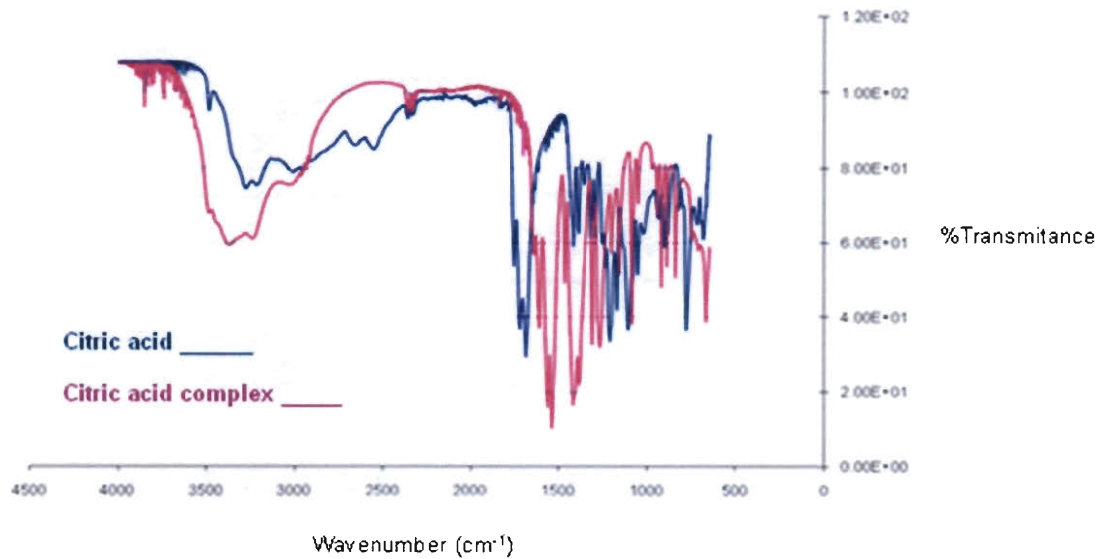


**Figure 1.24.** IR of citric acid and citric acid complex.

-like or lipid-like molecule.

Both the human samples and our model materials suggest that the Si:Ca ratio can vary over a range of at least 0.2 – 2.0 without significant alteration in morphology other than the size of the spherical structure. The identity of the silicon source in our model compounds appears to be flexible to some extent as shown by similarities of samples prepared with silica or silicones. Certainly, the potential of silicones as a nidus can be related not only to silicone oils used in surgery, but also silicones present in the production process and packaging for a wide range of products including ophthalmic drops.

The choice of SDS as a surfactant additive was based upon our prior experiences; however, our results suggest that the identity of the surfactant is less important than its presence. Thus, we suggest that any lipid-like molecule comprising a charged functional group (e.g., sulphate, phosphonic acid, carboxylic acid, etc) and an aliphatic

(hydrophobic) tail will be sufficient. Furthermore, the presence of a mixture of organic non-polar compounds that are present in the human eye also appears to be flexible, as indicated by the ability to generate suitable structures in the presence of hexane.

We have shown that a silicon source and calcium carbonate mixed with water in the presence of a surfactant molecule under physiological pH and temperature produces a substance that resembles biological calcium band keratopathy samples, and thus providing insight to the conditions necessary for deposit formation. In addition, we have developed a way to mimic the morphology and composition of the biological samples that allows for mass production of the material furthering the advances of therapeutics targeting CBK. This model has enabled us to further our study in search of a lead for new more patient friendly therapies for CBK.

Our studies for medicinal effect of nitrilo-*tris*(methylene)phosphonic acid,  $N[CH_2PO(OH)_2]_3$  ( $H_6ntmp$ ), revealed that this compound is highly effective at the complexation and extraction of calcium material from our synthetic model. Citric acid, our other calcium extracting candidate, also showed to be extremely efficient in dissolution of our synthetic sample. Despite our initial observation of fructose ability to dissolve fume silica, our studies on our synthetic CBK sample did not reveal similar results. No dissolution or surface topography change was observed. Further research in the applicability of  $H_6ntmp$  and citric acid as therapeutic agents on human CBK samples is of great importance and looks very promising.

Further investigation into medicinal effect of these two complexing agents on the human CBK precipitates is essential. To ascertain the safety and toxicity aspects of these agents, and their applicable dosage for human eye, in-vitro cell studies are needed. The effect of the slightly acidic solution (pH of 6.5) in the neutral environment of the eye must also be determined. The emerging therapeutic drugs may bear some unknown

factors along with lack of long term exposure risks but generally their curative benefits could overcome their drawbacks.

### **Experimental**

Calcium carbonate, fumed silica, sodium dodecyl sulfate (SDS), tetradecylphosphonic acid (TDPA), silicic acid, silicon oil, and dodecane were purchased from Sigma-Aldrich. Hexane, hydrochloric acid and sodium hydroxide and D<sub>2</sub>O were purchased from Fisher Scientific. Carbon dioxide was purchased through Matheson Trigas. Ultra pure (UP) water was obtained from a Millipore Milli-Q UV water filtration system. All reagents were ACS grade or better and were used as received. Human eye samples were obtained from patients at the Cullen Eye Institute at Baylor College of Medicine, Houston, TX.

SEM images were observed on a FEI Quanta 400 ESEM. The samples were attached to a stub using carbon tape and then sputtered with a thin layer of gold to prevent charging. Powder X-ray diffraction studies were performed on a Rigaku diffractometer. Samples were attached to a glass slide using a 5 - 100° angle range. XPS data was acquired on a Phi Quantera system using an aluminum X-ray at a 45° angle. Raman data was collected on a Renishaw Raman Microscope with a 785 nm laser power.

**Precipitation reaction of calcium carbonate without hydrocarbon.** A summary of experimental variations is given in Table 1. An appropriate quantity of CaCO<sub>3</sub> was added to deionize water (100 mL). This solution was then allowed to stir in an oil bath at 36 °C for one hour with CO<sub>2</sub> bubbling through the solution. After an hour, silicon reagent and/or surfactant were added to the calcium solution and stirring resumed at 36 °C with CO<sub>2</sub> bubbling again for a time period ranging from 4 to 24 hours. The

reaction was then allowed to rest without stirring but in a heated environment for 24 h. The resulting precipitate was collected by vacuum filtration.

**Precipitation reaction of calcium carbonate in the presence of hydrocarbon.**

A solution of  $\text{CaCO}_3$  was prepared by dissolving a determined quantity of  $\text{CaCO}_3$  in deionized water (100 mL). The solution was then stirred at 36 °C for an hour while  $\text{CO}_2$  bubbled through the solution. Then, the silicon reagent, surfactant, and hydrocarbon were added to this solution and stirring resumed at 36 °C with  $\text{CO}_2$  bubbling again. The reaction time and amounts of reagents varied according to Table 2. The reaction was then allowed to sit with heat for 24 h and the resulting precipitate was collected by vacuum filtration.

It must be noted that multiple samples of each set of precipitated were grown in order to confirm the reproducibility of the methods. In each case the elemental analysis was within experimental error and the morphologies were identical.

**Vertical scanning interferometry.** Solutions of 5% sample **20** was placed and fixed in a commercial epoxy resin and allowed to dry overnight. Resin was then cured at 125 °C and 176 °C, respectively, and the surface was polished. The fixed sample was mounted with constant orientation and position on the interferometer's stage. Sample was then reacted with a flowing solution of fixed composition for discrete time intervals, solution was dried after each time interval and VSI surface topography measurements were acquired. The change in surface topography of sample surface was monitored using 10x objective which allows mapping of a relatively large area of the sample surface (~0.5 mm<sup>2</sup> field of view) at subnanometer vertical resolution. Surface topography images were also taken at 80x objective as well. For VSI measurements, 5% solutions of  $\text{H}_6\text{ntmp}$ ,

citric acid and fructose in DI water were prepared and pH was adjusted to 6.5 with NaOH or HCl.

**NMR and IR spectroscopy.** Solution  $^{31}\text{P}$  NMR spectra were obtained on a Bruker Avance 400 MHz spectrometer at 161.9 MHz. Proton-decoupled spectra were collected using a 9.6- $\mu\text{s}$  pulse based on  $90^\circ$  pulse width calibrations with 85% phosphoric acid and a 3.0 s relaxation delay. The samples were externally referenced to 85%  $\text{H}_3\text{PO}_4$  at 0.0 ppm. IR spectra were obtained using a Nicolet FTIR spectrometer.

## References

- 1 H. F. W. Taylor. *Cement chemistry*, Academic Press; 1997.
- 2 M. Bishop and A. R. Barron, *Ind. Eng. Chem. Res.*, 2006, **15**, 3074.
- 3 C. Lupu, R. S. Arvidson, A. Luttge, and A. R. Barron, *Chem. Commun.*, 2005, 2354.
- 4 E. Shorr, T. P. Almy, M. H Sloan, H. Taussky, and V. Toscani, *Science*. 1942, **96**, 587.
- 5 L. L. Hamm, *Kidney International*, 1990, **38**, 728.
- 6 R. R. Pfister, J. L Haddox, and K. M. Lank, *Investigative Ophthalmology & Visual Science*, 1988, **27**, 1110.
- 7 N. Doostdar, C. J. Manrique, M. B. Hamill, and A. R. Barron. Submitted for publication.
- 8 F. Walker and R. S. Patrick, *Exp. Eye Resm*, 1967, **3**, 227.
- 9 P. Klugeres, F. Kopp, and V. Martin, *Chem.. Eur. J.*, 2004, **10**, 4538.
- 10 W. Bowman, *Lectures on the parts of concerned in the operations on the eye, and on the structure of the retina*, 1849.
- 11 A. J Dark and J. Proctor, *British.J. ophthalmology*, 1982, **66**, 309.

- 12 M. Ni and B. D. Ratner, *Surf. Interface Anal.*, 2008, **40**, 1356.
- 13 E. M Carlisle, *Science*, 1970, **116**, 711.
- 14 C. Lupu, K. L. Jackson, S. Bard, I. Rusakova, and A. R. Barron, *Adv. Eng. Mater.*, 2006, **8**, 576.
- 15 D. Borchman, G. N. Foulks, M. C. Yappert, and D. V. Ho, *Biopolymers*, 2007, **87**, 124.
- 16 E. A. Whitsitt and A. R. Barron, *J. Colloid. Interface Sci.*, 2005, **287**, 318.
- 17 R. E. Anderson and A. R. Barron, *Main Group Chem.*, 2005, **4**, 279.
- 18 E. Baeuerlein, *Biomineralization From biology to biotechnology and medical application*, Wiley-VCH, 2000.
- 19 M. M. Cortalezzi, V. Colvin, and M. R. Wiesner, *J. Col Int. Sci.*, 2005, **283**, 366.
- 20 E. A. Whitsitt and A. R. Barron, *Chem. Comm.*, 2003, 1042.
- 21 E. A. Whitsitt and A. R. Barron. *Nano Lett.*, 2003, **3**, 775.
- 22 H. Baumann, *Beitr. Silikose-Forsch*, 1960, **4**, 19.
- 23 J. L Federman and H. D Shubert, *Ophthalmology*, 1988, **95**, 870.
- 24 P. K. Leaver, R. H. B. Grey, and A. Garner, *Br. J. Ophthalmol.*, 1979, **63**, 361.
- 25 M. W. Dorey, S. Browstein, V. Hill, B. Matthew, G. Botton, P. Kertes, and S. El-Defrawy, *Am. J. Ophthalmol.*, 2003, **135**, 591.
- 26 A. M. Izak, L. Werner, S. K. Pandey, T. A. Macky, R. H. Trivedi, and D. J. Apple, *Int. Ophthalmol. Clin.*, 2001, **41**, 63.
- 27 N. E. Habib, T. J Freegard, G. Gock, P. L. Newman, and R. M Moate, *Eye*, 2002, **16**, 69.
- 28 A. Streitwieser, L. Heathcock, and E. Kosower, *Introduction to Organic Chemistry*, 4<sup>th</sup> Ed., 1998.

## Chapter 2

### Biological Effects of Functionalized Buckminsterfullerene (C<sub>60</sub>)

#### Introduction

This year marks the silver anniversary of the discovery of the most abundant, symmetrical and stable form of fullerene clusters, Buckminsterfullerene (C<sub>60</sub>). Following its discovery in 1985<sup>1</sup> and macroscopic-scale synthesis in 1990,<sup>2</sup> covalent functionalization of this nanosphere for various applications in diverse scientific fields ranging from material to biomedical sciences has burgeoned. The unique structural, physical, and photo-, electro-chemical properties of the C<sub>60</sub> core and its derivatives renders them particularly interesting for various biomedical and biotechnological applications. Some researchers have reported antioxidant and free radical scavenging and quenching properties of functionalized C<sub>60</sub> derivatives.<sup>3</sup> Other investigators have studied the therapeutic and diagnostic imaging capabilities of C<sub>60</sub> derivatives.<sup>4</sup>

Potent inhibitors of human immunodeficiency virus type I aspartic protease (HIV-1 P) have been developed and used as drugs, however, the nature of majority of these drugs is peptide-like rendering limited oral bioavailability and half-life.<sup>5</sup> In search of more efficient and non-peptidic inhibitors of HIV-1 P enzyme, the particular size and geometrical shape of C<sub>60</sub> fullerene draw researchers attention. Initial molecular modeling studies revealed it as an ideal inhibitor of this enzyme, especially if additional interactions, besides hydrophobic interactions can be obtained.<sup>6</sup> The active site of the HIV-1 P is approximately an open-ended cylindrical hydrophobic cavity with a diameter of about 1 nm.<sup>5</sup> There are hydrophobic and hydrophilic amino acid residues inside the cavity of the HIV-1 P enzyme. Derivatization of the fullerene at specific positions with groups that may give hydrophobic or electrostatic interactions with these amino acids may increase the inhibitory effects of these derivatives considerably. Many fullerene

derivatives have since been synthesized and tested against HIV-1 P by several experimental groups.<sup>7</sup> The most active fullerene-based inhibitor currently available has an inhibitory binding ( $K_i$ ) of 103 nM.

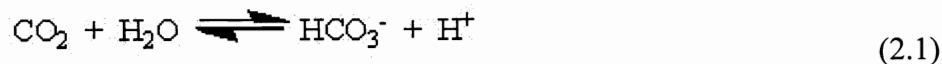
Molecular docking simulations, performed by our collaborators, revealed particular promise for a group of fullerene-based amine and amino acid derivatives that were formerly synthesized and characterized by our group.<sup>8</sup> Considering the theoretical observed significant inhibitory effects of these fullerene derivatives and the urgent need for new anti-HIV drugs, we synthesized these series of  $C_{60}$  derivatives in order to further study their inhibitory effects against HIV-1 P experimentally.

Hydrophobic cleft is a characterizing feature of the active site of many enzymes. Therefore,  $C_{60}$  may be envisioned as fitting these clefts and through intermolecular interactions provide a significant inhibitory effect. Indeed,  $C_{60}$  derivatives have shown inhibit activity against various other enzymes.<sup>9</sup> As a part of this research, we became interested in studying potential inhibitory effects of our fullerene derivatives for a group of carbonic anhydrase enzymes.

Carbonic anhydrases (CAs) form a family of metalloenzymes that catalyze conversion of carbon dioxide and water to bicarbonate and protons (Eq. 2.1). This simple reaction is very crucial in physiological processes connected with respiration and transport of  $CO_2$ /bicarbonate between tissues and lungs, pH and  $CO_2$  homeostasis, electrolyte secretion in a variety of tissues/organs, biosynthetic reactions, bone resorption, calcification, tumorigenicity, and many other physiologic or pathologic processes.<sup>10</sup> Therefore, CA enzymes have recently emerged as potential novel therapeutic targets for design of inhibitors to treat a range of disorders including glaucoma, obesity, cancer, epilepsy, and osteoporosis.<sup>10</sup> The  $\alpha$ -CAs,  $\beta$ -CAs,  $\gamma$ -CAs, and  $\delta$ -CAs are all members of the CA enzyme family. At least 16 isozymes of  $\alpha$ -CAs have been identified in mammals with very different subcellular localization and tissue distribution. These mammalian



isozymes are divided into four subgroups according to their location or distribution: the cytosolic forms, the membrane-bound isoforms, the mitochondrial forms and a secreted isozyme.<sup>10</sup>



The opening of the active site cleft of the  $\alpha$ -CAs is about 1.5 nm and contains a zinc ion (Figure 2.1) which is coordinated to the imidazole rings of three histidine residues, His 94, His 96 and His 119, and a hydroxide ion (not shown). With a diameter of about 1 nm, C<sub>60</sub> fullerene might be an interesting candidate to be investigated for its interaction with CAs. In fact, prior to this research, fullerene and its derivatives had not been studied for their interactions with CAs. Therefore, we investigated, in the course of a joint effort, whether our fullerene-based amine and amino acid derivatives may show inhibitory activity against all mammalian isoforms.

In drug development, disease diagnosis and disease treatment, the ability of the therapeutic and diagnostic moieties to selectively reach the desired targets with marginal or no collateral damage is of the utmost importance. An ideal therapeutic or imaging contrast system would also encompass the ability to overcome the biological barriers that prevent it from reaching its target.<sup>11</sup> C<sub>60</sub> fullerene materials have been studied for use in nanomedicine and show great promise for crossing cell membranes and even producing transfection.<sup>12</sup> Previous research conducted by our group has shown the transport of a fullerene based amino acid-peptide conjugate into a cancer cell.<sup>13</sup> In this conjugate system, the fullerene acted as a passport for intracellular delivery of peptide into the cell where the peptide in the absence of the fullerene amino acid could not enter the cell. This fullerene based amino acid-peptide conjugate was also capable of inhibiting proliferation of neuroblastoma cells at low concentration.<sup>13</sup>

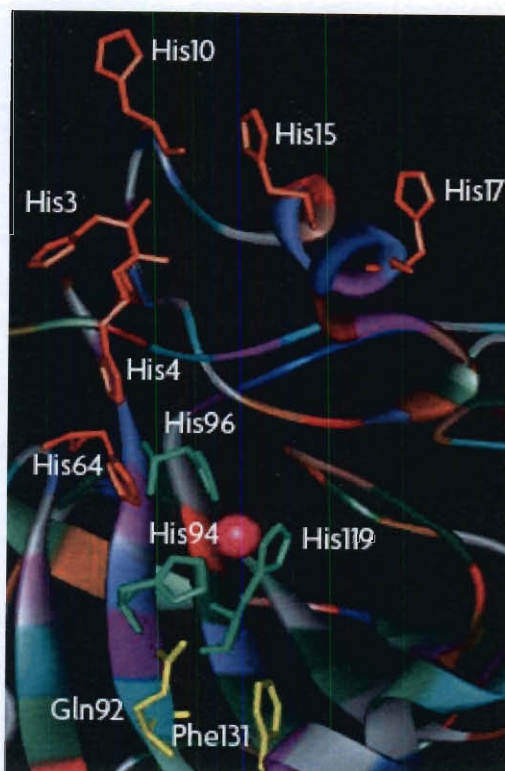


**Figure 2.1.** Active site of  $\alpha$ -CA enzymes ( $Zn^{2+}$  is shown as a pink sphere and histidines in green).<sup>10</sup>

Neuroblastoma is the most common extracranial solid tumor in infants and young children and accounts for about 15% of pediatric cancer death. Despite advances in treatment options, aggressive neuroblastomas remain unmanageable and additionally, current therapies present significant acute and chronic drug toxicity. Among the biological markers that have been identified in patients with neuroblastoma, *N-myc* oncogene is the most important one.<sup>14</sup> *N-myc* is amplified in approximately one quarter of neuroblastoma cases and is more common in patients with advanced stage disease. Overexpression of this oncogene is associated with rapid tumor progression and a poor prognosis for patients.<sup>14</sup> Identification of effective and selective inhibitors of *N-myc* would be important for the development of therapeutic agents for neuroblastoma. A

major clinical limitation of currently designed inhibitors of *N-myc* is their rapid degradations.<sup>15</sup> Our fullerene based amino acid-peptide conjugate showed no degradation when exposed to bovine plasma suggesting that fullerene amino acid linkage to peptide might be stable under physiological conditions.<sup>13</sup> Considering the promising features of our reported fullerene based amino acid-peptide conjugate, we identified and synthesized a series of potential inhibitory fullerene peptides derived from the H1 binding domain of the *N-myc* protein that can bind with this domain and restrain its amplification.

### Result and Discussion

All C<sub>60</sub> derivatives for HIV and CA inhibition studies were prepared and characterized according to previously reported methods (Figure 2.2).<sup>8</sup>

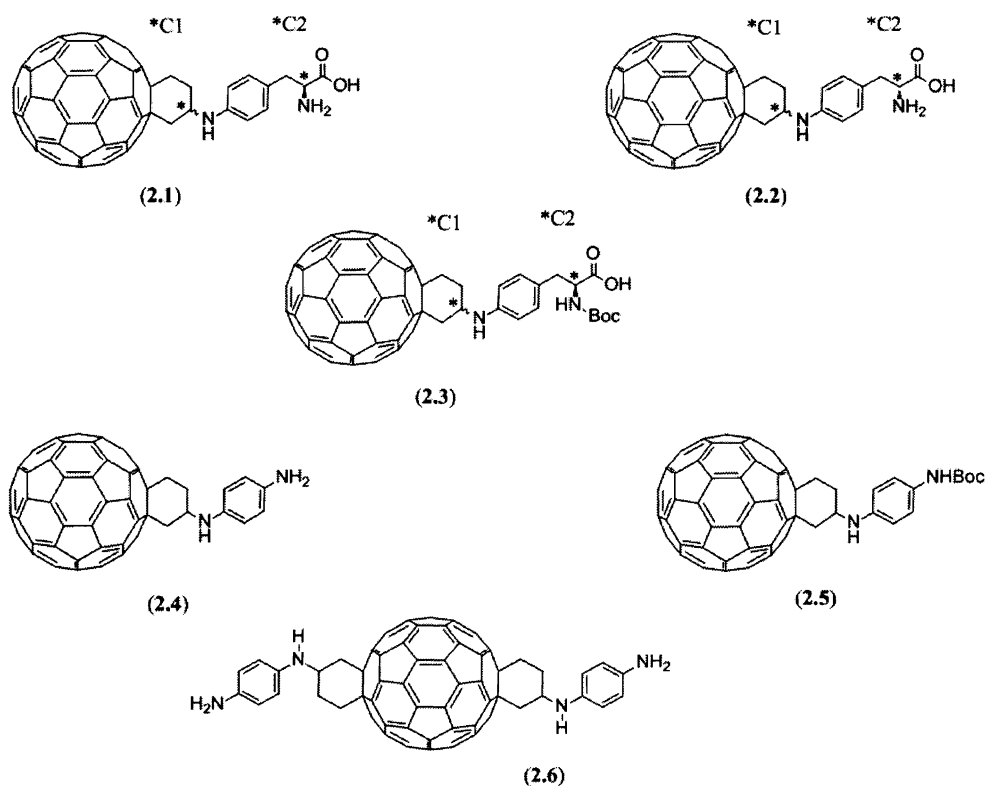
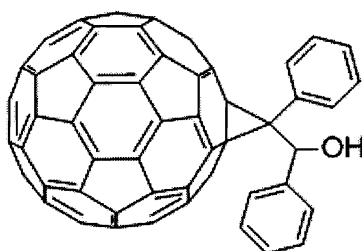


**Figure 2.2.** Compounds synthesized for HIV-1 P and CAs inhibition studies.

**HIV inhibition studies.** Molecular docking simulation studies conducted by our collaborators showed that compounds **2.1** through **2.6** have higher or slightly lower affinity for HIV-1 P in compare to previously reported fullerene derivatives. The higher affinities are connected with the ability of pendant groups to form H-bonds with the catalytic site of the enzyme as well as the van der Waals interactions between the fullerene cage and the nonpolar surface of active site amino acid residues. The binding scores of these fullerene derivatives were comparable to the reported most potent fullerene-based HIV-1 PR inhibitor (**I**). Subsequent biological tests were performed for these compounds. The results of the computational and biological studies are summarized in Table 2.1. Compounds **2.1** and **2.2** showed relatively similar binding energies to the currently reported most potent fullerene-base HIV-1 P inhibitor, diphenyl C<sub>60</sub> alcohol, **I** both computationally and experimentally.



(I)

There are two chiral centers \*C1 and \*C2 at compounds **2.1**, and **2.2** and **2.3** (Figure 2.2); \*C2 has an (S) configuration in compound 2.1 and 2.3 and (R) configuration in compound **2.2**, but \*C1 can have both configurations. Thus, both (S) and (R) configurations have been taken into consideration in the docking simulations. It was noted that compounds that have an (S) configuration at \*C1 show slightly better binding energies than the corresponding (R) configuration (~1 - 4 kJ/mol) (Table 2.1). The

position of the best binding energy poses from molecular docking simulations of compound **2.1** with (S) and (R) configurations at \*C1 is similar at the binding pocket of HIV-1 PR. This compound with an (S) configuration at \*C1 forms four H-bonds with Arg8 and Asp30'; and compound with an (R) configuration at \*C1 forms three H-bonds with Arg8, Asp30', and Gly48' (Figures 2.3 and 2.4). In addition, van der Waals interactions are observed between the nonpolar unsubstituted fullerene cage of this compound with nonpolar moieties of residues such as Leu23, Ala28, Val32, Ile47, Ile50, Gly52, Phe53, and Pro81 of HIV-1 PR.

**Table 2.1.** Comparison of experimental and computational binding energies the fullerene derivatives at HIV-1 P.

Compound	Binding Energy (kJ/mol)	
	Computational	Experimental
<b>I</b>	-36.66	-40.13
<b>2.1</b>	-37.60 (*C1, S)	-39.75
<b>2.1</b>	-36.56 (*C1, R)	-39.75
<b>2.2</b>	-35.81	-39.67
<b>2.3</b>	-33.23	-36.52
<b>2.4</b>	-30.82	-29.75
<b>2.5</b>	-31.3	<-28.72
<b>2.6</b>	-26.8	<-28.72

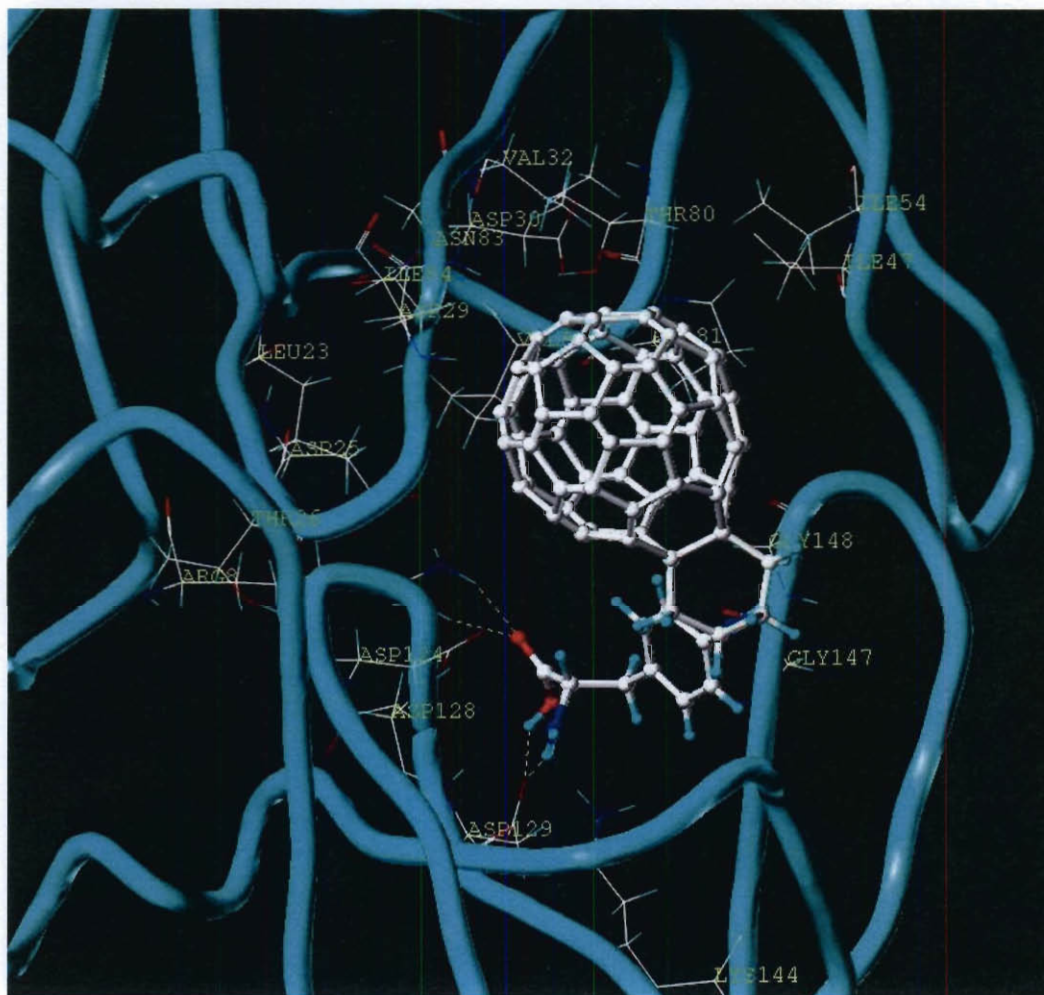


**Figure 2.3.** The binding interactions of compound **2.1** with (S) configuration at \*C1 with the active site residues of HIV-1 P.<sup>19</sup>

For comparison purposes, docking simulations were performed for compound **I** as well. These simulation showed that compound **I** forms only two H-bonds with Asp25' and Ala28' (Figure 2.5). The van der Waals interactions of its nonpolar surface are observed with nonpolar segments of HIV-1 PR residues (e.g., Leu23, Ala28, Val32, Ile47, Ile54, Pro81, Val82, and Ile84). In addition, compound **I** shows van der Waals interactions between its phenyl substituent with Val82'. The presence of multiple

functional group on of our fullerene derivatives offers the opportunity of further derivatization of these fullerenes which may improve their inhibitory effects considerably through increased hydrophobic or electrostatic interactions with the hydrophobic and hydrophilic amino acid residues of the enzyme's active site. These results and features of our fullerene derivatives show that new leads can be discovered possessing higher bioactivity against HIV-1 P.

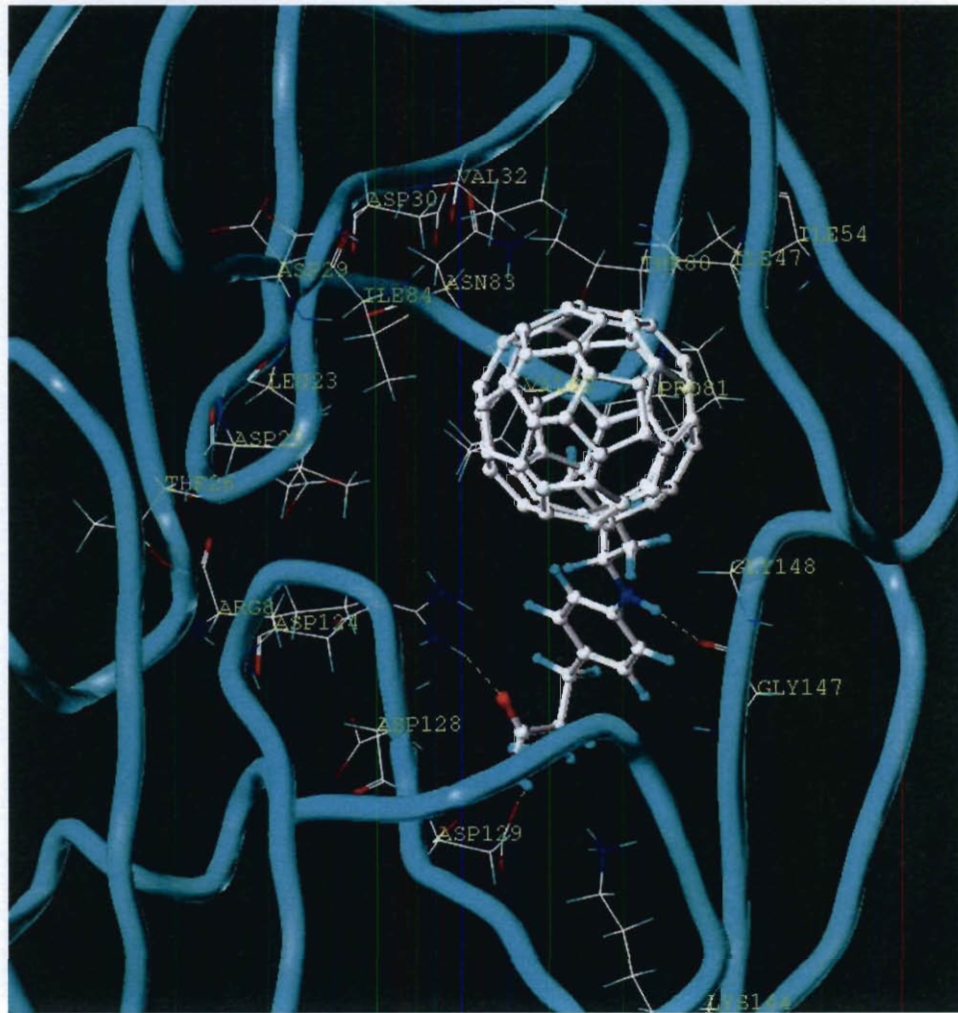


**Figure 2.4.** The binding interactions of compound **2.1** with (R) configuration at \*C1 with the active site residues of HIV-1 P.<sup>19</sup>

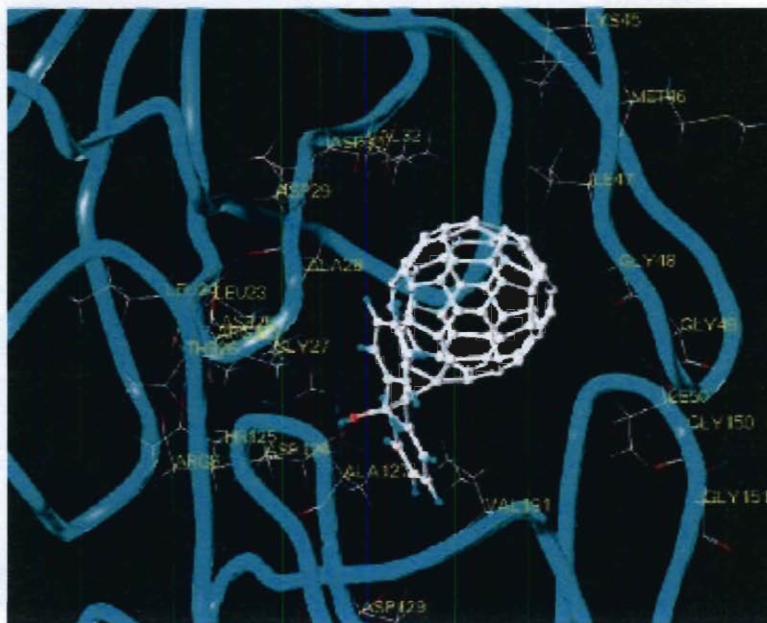


**Figure 2.5.** The binding interactions of compound **I** with the active site residues of HIV-1 P.<sup>19</sup>

**CAs inhibition studies.** All compounds listed on Figure 2.2, except compound **2.2**, and compound **I** were investigated for CAs inhibition by our collaborators. Inhibition data for these compounds against all 13 catalytically active mammalian (h = human, m = murine) CA isoforms, CA I–IV, VA, VB, VI, VII, IX, XII–XV, are presented in Table 2.2. Several CA isozymes were potently inhibited by all our fullerene derivatives, with inhibition constants in the submicromolar range ( $K_i$ s of 0.61–0.93  $\mu\text{M}$ ), among which are the tumor-associated hCA XII, and the transmembrane ones hCA XIV and mCA XV. The structure–activity relationship (SAR) is quite straightforward, with all derivatized fullerenes showing good activity. For example, the best inhibitor against hCA XII was the *p*-phenylenediamine derivative **2.4** ( $K_i$  of 0.61  $\mu\text{M}$ ). The protection of the amino group with the Boc moiety, as in **2.5**, or the bis-phenylenediamine **2.6** led to a slightly diminished activity compared to **2.4**. The same is true for the bulkier compounds **2.1**, and



**2.3** as well as for the compound **I**, but these derivatives also showed considerable hCA XII inhibitory activity. Compound **I** was the inhibitor for HCA XIV.

**Table 2.2.** Inhibition of mammalian carbonic anhydrase isozymes with fullerene derivatives.

Isozyme	Ki ( $\mu\text{M}$ )					
	<b>2.1</b>	<b>2.3</b>	<b>2.4</b>	<b>2.5</b>	<b>2.6</b>	<b>I</b>
hCA I	8.82	9.31	9.63	9.54	7.95	7.57
hCA II	9.05	9.38	9.38	8.75	6.73	16.6
hCA III	9.58	9.42	8.77	8.91	8.23	8.9
hCA IV	7.04	12.3	6.44	11.5	94.5	3.66
hCA VA	111	94.4	51.8	50.3	85.9	49.7
hCA VB	87.6	28.6	40.6	27.7	64.5	38.3
hCA VI	5.98	6.07	0.89	5.91	1.04	0.87
hCA VII	10.6	10.94	9.82	10.58	12.59	10.31
hCA IX	13.4	14.32	12.9	11.07	12.87	7.93
hCA XII	0.67	0.76	0.61	0.66	0.73	0.73
hCA XIII	7.64	8.73	8.75	8.78	8.71	7.57
hCA XIV	0.9	0.88	0.93	0.89	0.84	0.77
mCA XV	0.83	0.81	0.9	0.89	0.82	0.82

h = human, m = murine isoforms.

The only secreted isoform, hCAVI, showed a more intricate inhibition profile with the fullerenes. Indeed, the less bulky compound **2.4** was submicromolar inhibitors

( $K_i$ s of 0.87 – 0.89  $\mu\text{M}$ ), the bisamine **2.6** had a  $K_i$  of 1.04  $\mu\text{M}$ , whereas the remaining compounds were less inhibitory, with  $K_i$ s in the range of 5.91–8.50  $\mu\text{M}$ . In this case it may be stated that the compounds with more compact moieties (such as **2.4**, and **2.6**) were the best inhibitors.

A large number of CA isozymes such as hCA I, II, III, VII, and XIII (cytosolic CAs) and the tumor-associated transmembrane and tumor-associated CA IX were inhibited by all our fullerenes in the low micromolar range, with inhibition constants typically in the range of 7 – 15  $\mu\text{M}$ . The ubiquitous and catalytically very efficient hCA II was best inhibited by the bisamine **2.6**. hCA VII was slightly less susceptible to this fullerene class of inhibitors compared to hCA I. The tumor-associated hCA IX showed inhibition constants with all fullerenes in the range of 7.93 – 14.32  $\mu\text{M}$ . The best hCA IX inhibitor was compound **I**, whereas the least effective one was the Boc-substituted Phe derivative **2.3**. Thus, even for a small series of derivatives relatively minor structural changes influence the CA inhibitory activity significantly, this is promising in designing a totally new class of inhibitors.

The extracellular isoform hCA IV, similar to hCA VI, shows a very typical and unique inhibition profile with these compounds ( $K_i$ s in the range of 3.66 – 94.5  $\mu\text{M}$ ). Thus, the bisamine **2.6** is a very ineffective hCA IV inhibitor, whereas compound **2.4** is effective one. Thus, the difference of activity between the two structurally related compounds **2.4** and **2.6** is important, with the monoamine **2.4** being 14.7 a better hCA IV inhibitor compared to the bis-derivative **2.6**. The remaining compounds 4–6 showed an intermediate activity between these extremes, with  $K_i$ s in the range of 7.04 – 12.30  $\mu\text{M}$ .

The two mitochondrial isoforms hCA VA and hCA VB were the least inhibited ones by the fullerenes 1 – 7. Indeed, these compounds showed inhibition constants in the range of 27.7 – 111  $\mu\text{M}$  against these two enzymes.

All these data clearly show that each of the 13 catalytically active CA isozymes has a particular inhibition profile with our fullerenes. Furthermore, the SAR for this small series of derivatives is rather complex, with a range of inhibition constants from the submicromolar to submillimolar, which makes this class of derivatives of particular interest in developing nanoscale CAIs.

Molecular docking studies were performed by our collaborator in order to investigate the interactions between fullerenes and amino acid residues within the CA active site. Two CA isozymes (CA II and CA IX) were used in these docking studies. For both CA isoforms, the fullerene binds in similar active site region, as shown in Figure 2.6. Docking binding scores for these fullerenes within the CA II and IX active sites varied between  $-6.02$  kcal/mol and  $-9.36$  kcal/mol (i.e., from micromolar to submicromolar binding affinity, Table 2.2), which is within the same range as those obtained experimentally Table 2.3.

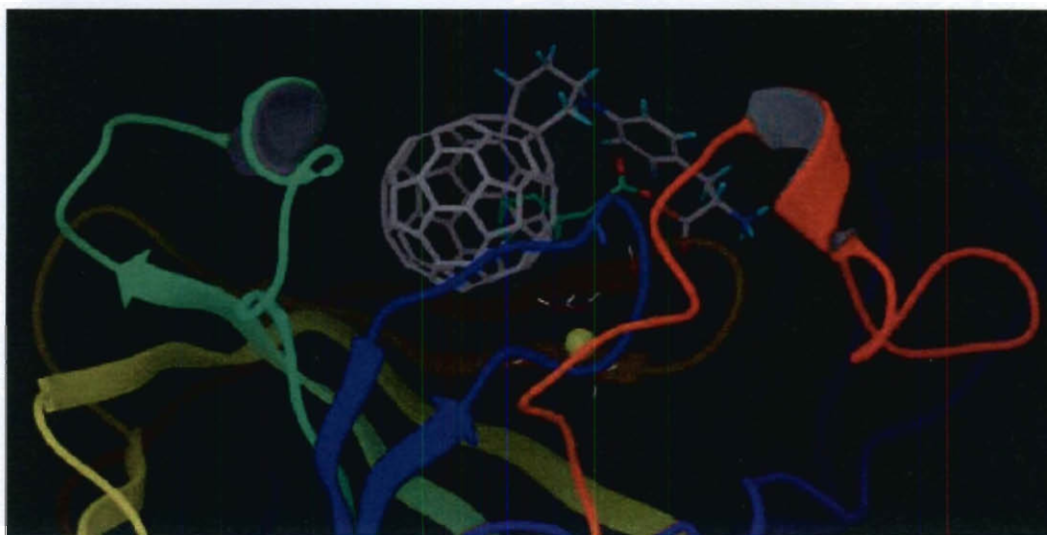


**Figure 2.6.** Binding of fullerene 2.1 to hCA II (shown as ribbon representation of the amide backbone). The catalytic Zn(II) ion is the yellow sphere at the center of the molecule.<sup>20</sup>

**Table 2.3.** Computational binding energies of fullerene derivatives to CA II and CA IX.

Compound	CA II (kcal/mole)	CA IX (kcal/mol)
<b>I</b>	-6.66	-7.90
<b>2.1</b>	-9.14	-6.63
<b>2.3</b>	-7.95	-8.47
<b>2.4</b>	-6.76	-6.02
<b>2.5</b>	-7.31	-6.03
<b>2.6</b>	-6.95	-6.49

The fullerene cage was observed to be located at the entrance of the CA active site when interacting with both CA isozymes, CA II and IX, thus occluding the entrance of substrates or other molecules within the cavity. The amino acid residues involved in these interactions were His64, His94, His96, Val121, and Thr200 (Figure 2.7). The docking studies showed that hCA II was best inhibited by compound **2.1**, whereas the worst inhibitor was compound **I**, which was found also experimentally to be the worst inhibitor of this isozyme. Thus, there is a good agreement between the experimental and computational studies regarding the interaction of hCA II/IX with fullerenes **2.1**, and **2.3** - **2.6**.

Compound **2.3** showed good inhibition against isozyme hCA IX. Its binding to this isoform is represented in Figure 2.8, as obtained by the docking procedure. Although compound **6** has similar binding scores with hCA II and IX, the location of the fullerene cage showed different locations within these isozyme active sites. In hCA II, the fullerene cage was located more outwards within the active site compared to its binding to the hCA

IX active site (Figure 2.9). Since the binding scores were similar for these two isozymes, this is a confirmation that the pendant groups present in the fullerene molecule have an important role in the inhibition of the diverse CA isozymes. Thus, the main finding of these molecular modeling studies is that the fullerene cage binds at the entrance of the CA active site and occludes it, inhibiting the enzymes in a manner similar to that of the coumarins, the recently discovered CAIs.<sup>16</sup> A second significant finding is that the pendant groups present in the fullerene derivative strongly influence the interaction of the inhibitor with amino acid residues found at the entrance of the active site cavity. As these residues are generally different between the various CA isozymes, this can lead to isoform-selective CAIs. This has been observed experimentally in the small library of derivatives investigated here and confirmed by means of the docking studies.

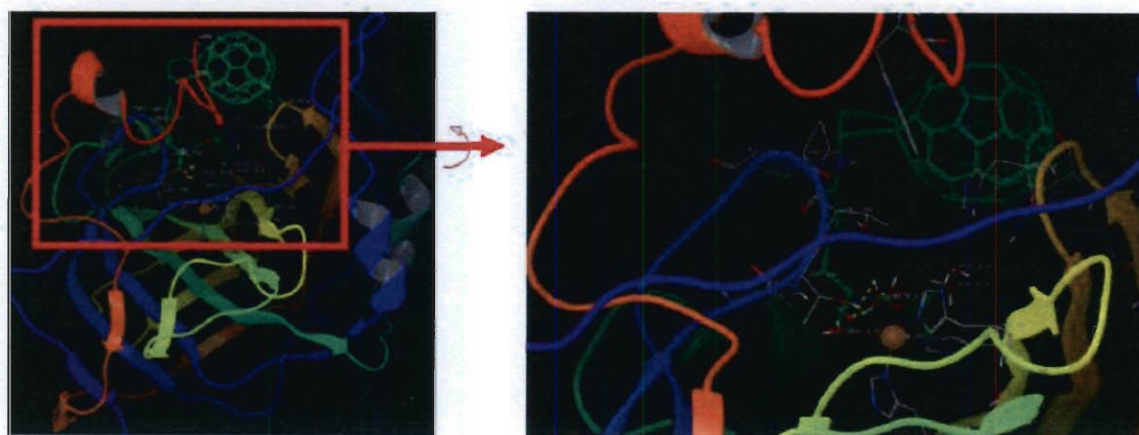


**Figure 2.7.** Binding of fullerene **2.5** to hCA II as obtained by the induced fit docking method. Yellow and green dashed bonds show H-bonds and close-van der Waals contacts, respectively. The catalytic Zn(II) ion is shown as orange spheres.<sup>20</sup>

**Neuroblastoma cell growth studies.** Myc-family proteins are transcription factors with an apparent role in transcription or DNA replication.<sup>17</sup> Elevation in the levels

of Myc proteins is associated with carcinogenesis. The Myc-family proteins contain a C-terminal region including a basic helix-loop-helix/leucine zipper (bHLH-LZ) motif (Figure 2.10). A recent study has identified that a 14-amino acid modified peptide derived from the H1 region of c-Myc can interfere *in vitro* with specific DNA binding and inhibits cancer cell growth.<sup>18</sup> Amino acid substitutions (mutations) at nonconserved residues were made in the helix-1 peptide of c-Myc with a strategy of conferring greater helical content to these peptides and increasing their heterodimeric function. Amino acids leucine and serine were substituted by alanine in order to provide helix stabilization in these peptides and which in turn provided a surprising inhibitory effect.

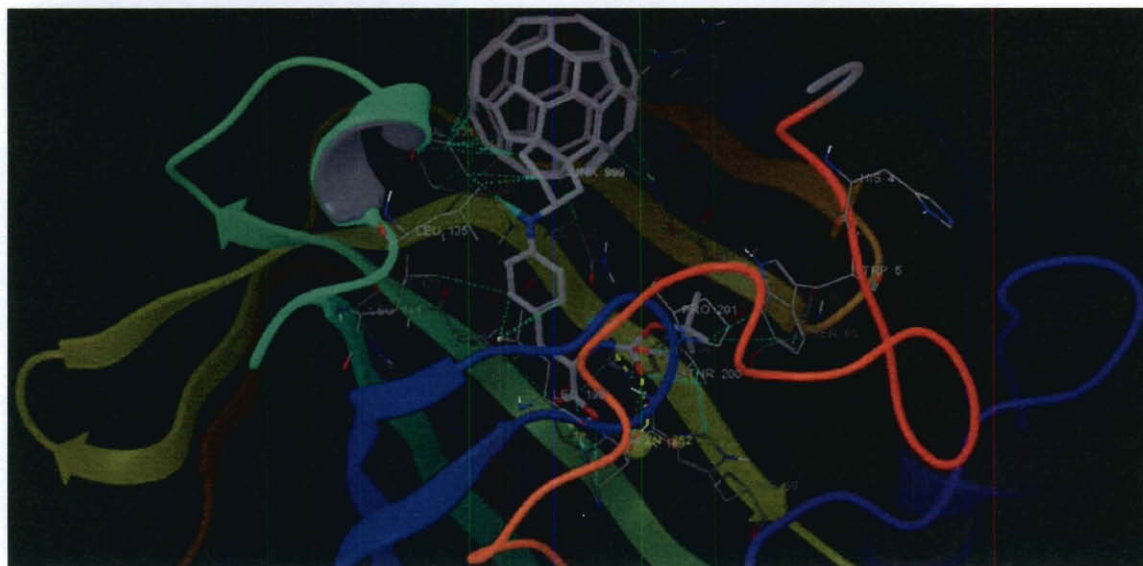


**Figure 2.8.** Binding of compound **2.3** to hCA IX. Yellow and green dashed bonds show H-bonds and close-van der Waals contacts, respectively. The catalytic Zn(II) ion is shown as the yellow sphere.<sup>20</sup>

Therefore, we chose the peptides for neuroblastoma inhibition studies from the H1 region of the n-Myc protein which is amplified in neuroblastoma cells and modified them accordingly. For each parent peptide sequence the fullerene substituted

phenylalanine (noted as **Baa** hereafter) peptide derivatives were also prepared and compared to their parent non-fullerene containing sequence. We investigated the effect of fullerene on the cellular uptake of these peptides and also whether these peptides show any inhibitory activity for neuroblastoma cell proliferation. To visualize the fullerene peptide inside the cells, fluorescein isothiocyanate (FITC) was introduced as a label. The fullerene derivatives were prepared by SPPS on preloaded crude peptide on wang resin. In the case of the parent sequences, a phenylalanine was coupled to the end to mimic the phenylalanine structure of the Baa residue.

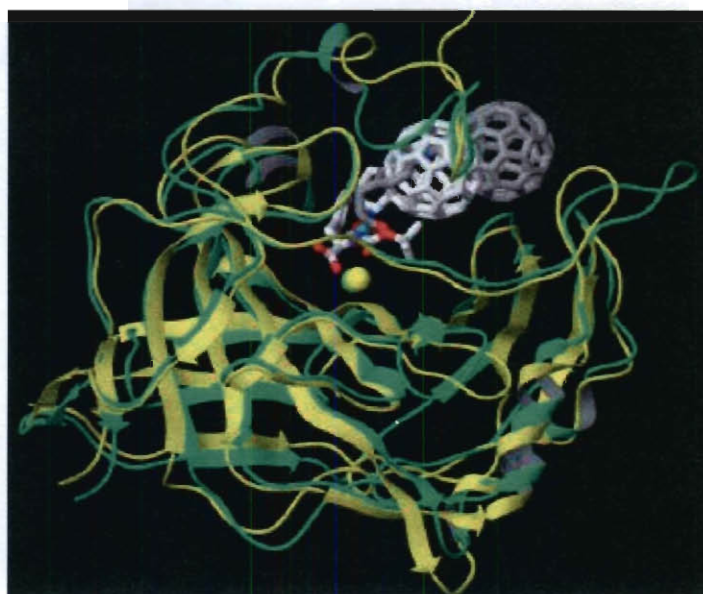


**Figure 2.9.** Superimposition of hCA II (shown in yellow colored ribbons) and hCA IX (shown in green colored ribbons) docking complexes of fullerene **2.3**. Dark colored fullerene shows the binding pose at hCA II and light colored fullerene shows the binding pose at hCA IX. The Zn(II) ion is shown by yellow (for hCA II) and green (for hCA IX) sphere, respectively.<sup>20</sup>



**Figure 2.10.** The basic helix-loop-helix/leucine zipper of Myc family proteins.<sup>18</sup>

All appropriate peptides were prepared according to previously reported methods and characterized by MALDI-TOF MS spectroscopy. MALDI-TOF mass spectra show the parent ion ( $M^+H$ ) and  $M^+H$ -FITC for each peptide. The specific sequences investigated along with the cell lines employed are in Table 2.4.

The cellular uptake study was conducted by our collaborators using JF cell lines. The fluorescence images of the parent peptides **2.9** revealed no significant uptake in the cells. However, the Baa analogue of that peptide, **2.12**, showed some localized intense fluorescence in the cytoplasm of the cells (Figure 2.11). It appears that the addition of the Baa residue to the sequence facilitated the intracellular localization of the peptide **2.12**.

The effect of the Baa-peptide sequences on the cell viability of SH-SY5Y neuroblastoma cells were investigated to determine if the sequence has an effect rather than the presence of the  $C_{60}$ . Exposure of SH-SY5Y cells to the Baa-peptides for 48 hrs showed no significant inhibition of cell growth by Baa-peptides **2.10** and **2.11**, but Baa-peptide **2.12** showed significant inhibition towards this cell line (Figure 2.12), specifically at 40  $\mu$ M. Clearly the sequence could have a significant effect on the cell viability, however, it must be noted that this result could be due to differences in the cellular uptake of these sequences or formation of aggregates in the cell.

A similar comparison has been made with the same cell line using the parent peptides **2.7 - 2.9** (Figure 2.13). The parent peptides **2.7** and **2.8** show no significant inhibition just like their Baa analogues while peptide **2.9** shows slight effect at the higher concentration (40  $\mu$ M) (Figure 2.13). This result could be an indication that the inhibition effect is indeed related to the peptide sequence not the presence of fullerene.



**Table 2.4.** Peptide sequences and cell lines studied.

Peptide	Sequence	Cell line <sup>a</sup>
2.7	F-K(FITC)-NDLRSSFLTLRDHV	SH-SY5Y, IMR32, MCF-7, LAN-1
2.8	F-K(FITC)-NDLRSSFATLRDHV	SH-SY5Y, IMR32, MCF-7, LAN-1
2.9	F-K(FITC)-NDLRSAFATLRDHV	JF, SH-SY5Y5, IMR32, MCF-7, LAN-1
2.10	<b>Baa</b> -K(FITC)-NDLRSSFLTLRDHV	SH-SY5Y, IMR32, MCF-7, LAN-1
2.11	<b>Baa</b> -K(FITC)-NDLRSSFATLRDHV	SH-SY5Y, IMR32, MCF-7, LAN-1
2.12	<b>Baa</b> -K(FITC)-NDLRSAFATLRDHV	JF, SH-SY5Y, IMR32, MCF-7, LAN-1

<sup>a</sup> SH-SY5Y, JF, IMR32 = neuroblastoma cancer cells, MCF-7 = breast cancer cell line.

A much unexpected result was observed when the inhibitory effects of the Baa peptides and their parent peptides were tested against the proliferation of neuroblastoma cell lines IMR-32 and LAN-1 and breast cancer cell line MCF-7. While none of the parent peptide show significant inhibitory effects, their Baa peptide conjugate activated the proliferation of these cells (Figure 2.14-2.16). Although we have not yet explored the underlying cause of this activation process, this effect if observed with other cell lines

might constitute a possible therapeutic approach for degenerative illnesses where cell growth is halted.

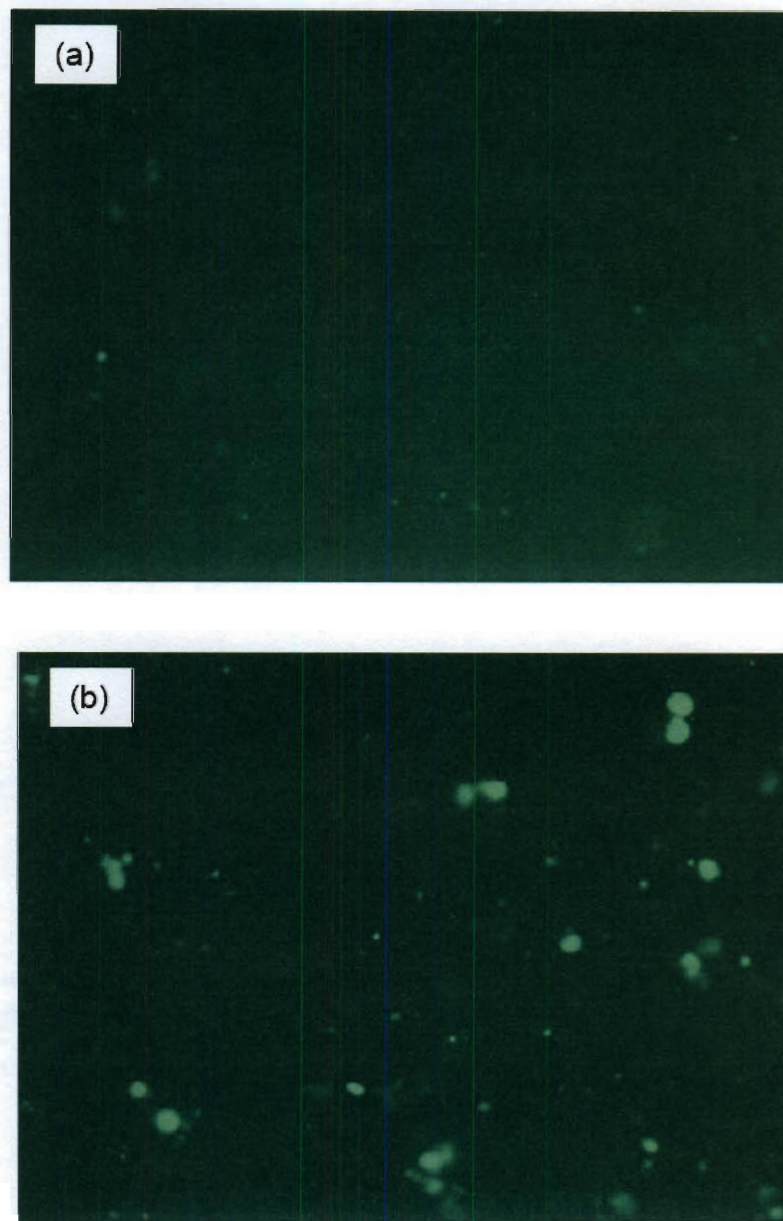


**Figure 2.11.** Fluorescence images of JF cell incubated with (a) F-K(FITC)-NDLRSAFATLRDHV and (b) Baa-K(FITC)-NDLRSAFATLRDHV.

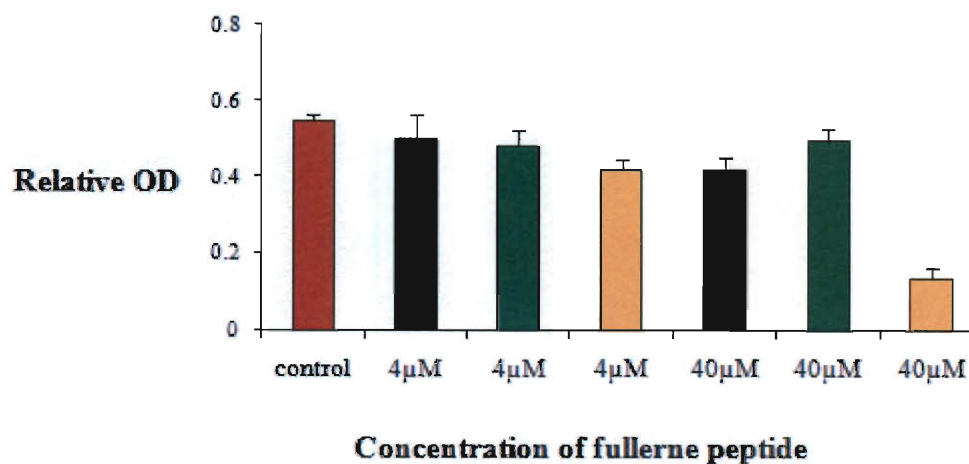


**Figure 2.12.** Inhibition of fullerene peptides against the proliferation of neuroblastoma cell line (SH-SY5Y), (2.10, ●), (2.11, ●), and (2.12, ●).

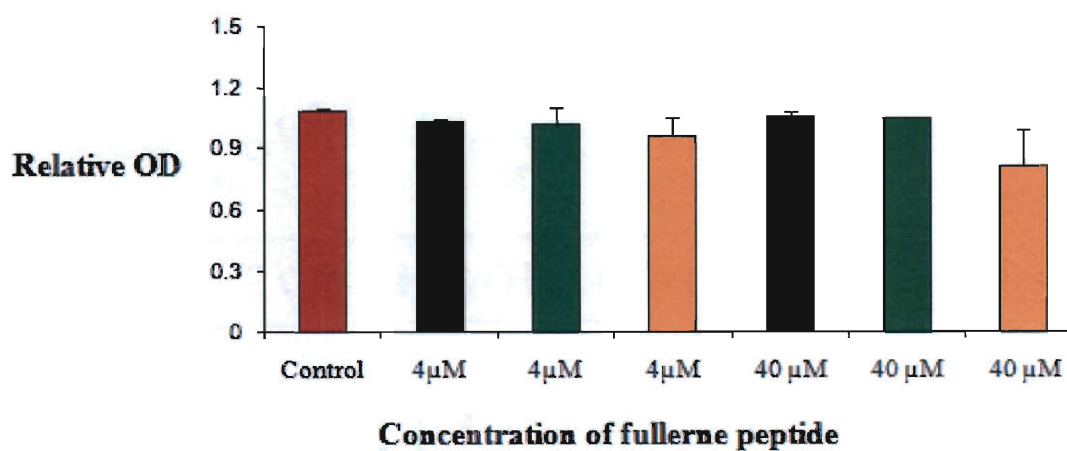


**Figure 2.13.** Inhibition of fullerene peptides against the proliferation of neuroblastoma cell line (SH-SY5Y), (2.9, ●), (2.10, ●), and (2.11, ●).

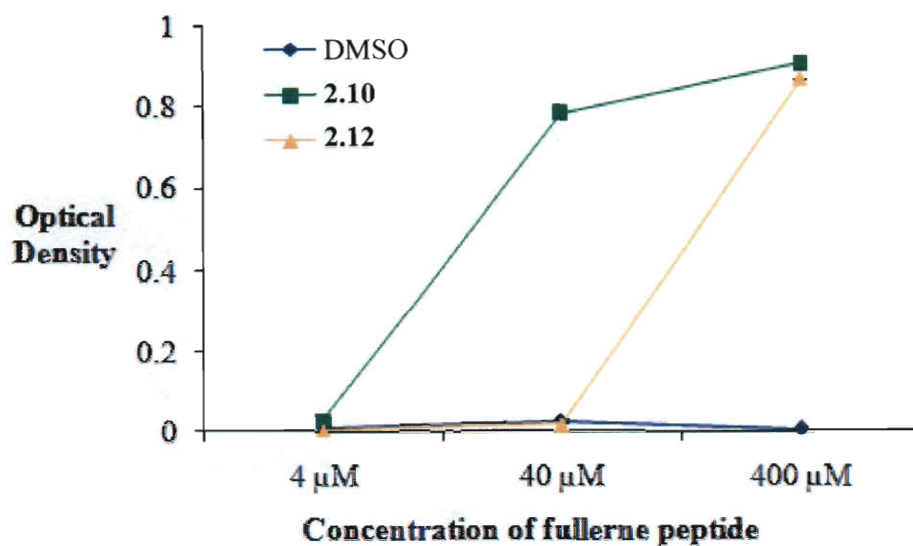


**Figure 2.14.** IMR-32 neuroblastoma cell line proliferation in DMSO, and Baa-peptides 2.10 and 2.12.

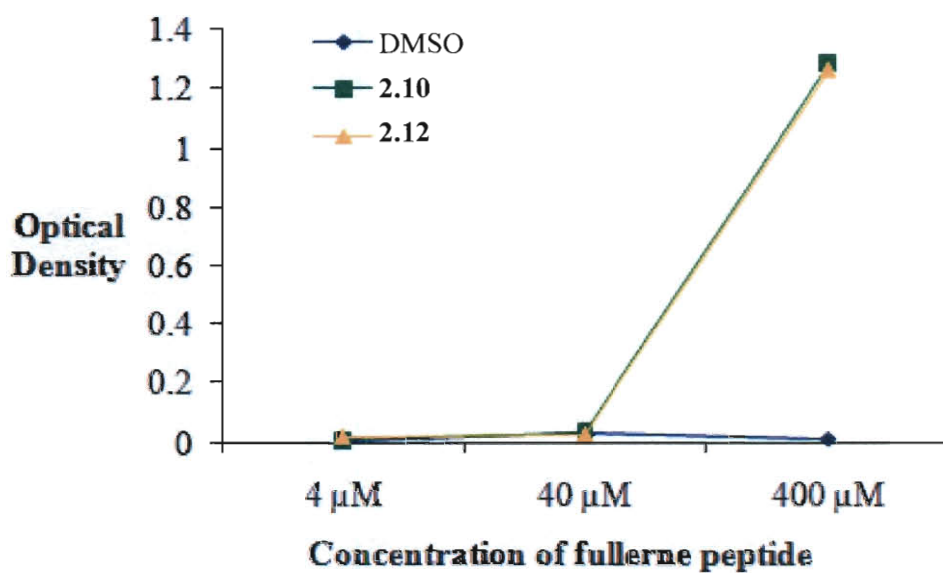


**Figure 2.15.** LAN-1 neuroblastoma cell line proliferation in DMSO, and Baa-peptides 2.10 and 2.12.

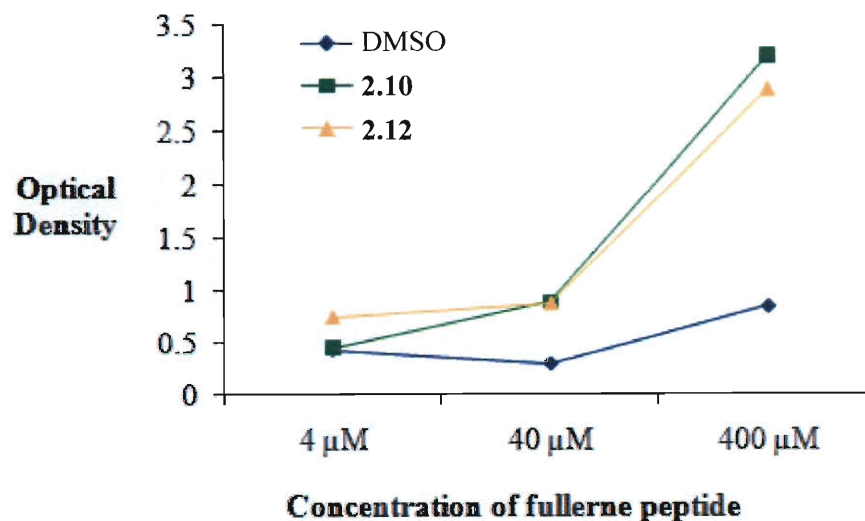


**Figure 2.16.** LAN-1 neuroblastoma cell line proliferation in DMSO, and Baa-peptides 2.10 and 2.12.

### Conclusions

In search of discovery and expansion of possible novel applications of our current library of fullerene materials, we have learned that a series of these functionalized fullerenes have anti-HIV activities similar to the most active fullerene based inhibitors currently available. The presence of multiple functional groups offers an opportunity for further functionalization of these series in order to amplify their inhibitory effect.

We discovered that these derivatives can also bind to thirteen different mammalian isoforms of CAs with submicromolar-low micromolar affinity. By means of computational methods the inhibition mechanism of the fullerene derivatives was identified as being due to occlusion of the active site by means of the fullerene cage (possessing dimension of the same order of magnitude with the opening of the enzyme cavity). The pendant moieties to the fullerene cage will then interact with amino acid residues from the active site. Fullerenes thus represent a totally new class of nanoscale

CA inhibitors which may show applications for targeting physiologically relevant isoforms, such as the dominant CA II and the tumor-associated CA IX, which represent established drug targets.

The reverse outcome of our fullerene peptides for inhibition of neuroblastoma cell proliferation was unanticipated. A more comprehensive and thorough investigation is required to understand and confirm the activating effects of these fullerene peptides.

### Experimental

Peptide sequences were purchased on resin from Biosynthesis Laboratory. Fullerene was purchased from MER and used as received. Amino acids and FITC were obtained from Novabiochem and used as received. MALDI-TOF mass analysis was performed on Autoflex MALDI-TOF. All solvents were dried before use. All C<sub>60</sub>-peptides for neuroblastoma inhibition studies were prepared and characterized by MALDI-TOF mass spectroscopy according to previously reported methods.<sup>13</sup> Purification of all peptides was carried out on an Phenomenex Luna C5 column using isocratic gradient of A: 0.1% TFA in water, B: 0.1% TFA in isopropanol, 70% B, at 5.0 mL/min flow rate.

**F-K(FITC)-NDLRSSFLTLRDHV (2.7).** MALDI-MS: *m/z* calculated 2355 [M<sup>+</sup>], 1965 [M<sup>+</sup>-FITC], found 2355 and 1965.

**F-K(FITC)-NDLRSSFATLRDHV (2.8).** MALDI-MS: *m/z* calculated 2314 [M<sup>+</sup>], 1924 [M<sup>+</sup>-FITC], found 2314 and 1924.

**F-K(FITC)-NDLRSAFATLRDHV (2.9).** MALDI-MS: *m/z* calculated 2298 [M<sup>+</sup>], 1908 [M<sup>+</sup>-FITC], found 2298 and 1908.

**Baa-K(FITC)-NDLRSAFATLRDHV (2.10).** MALDI-MS:  $m/z$  calculated 3127 [M<sup>+</sup>], 2737 [M<sup>+</sup>-FITC], found 3127, 2737.

**Baa-K(FITC)-NDLRSSFATLRDHV (2.11).** MALDI-MS:  $m/z$  calculated 3085 [M<sup>+</sup>], 2696 [M<sup>+</sup>-FITC], found 3085, 2696.

**Baa-K(FITC)-NDLRSSFLTLRDHV (2.12).** MALDI-MS:  $m/z$  calculated 3069 [M<sup>+</sup>], 2680 [M<sup>+</sup>-FITC], found 3069, 2680.

#### **Computational details and inhibition assays for HIV and CAs Studies.**

Computational methods and inhibition assay studies for HIV and CA inhibitions were performed by our collaborators and their detail is reported.<sup>19,20</sup>

**Preparation of fullerene peptide stock solution.** Lyophilized fullerene peptides and parent peptides were weighed and dissolved in PBS buffer (pH = 7) to make a stock solution of required concentration inside a clean hood for neuroblastoma inhibition studies.

**Cellular proliferation studies.** Inhibition studies for neuroblastoma cell proliferation were conducted at by our collaborator at BCM. Cancer cells at  $5 \times 10^3$  cells/well were plated in triplicate in standard flat bottomed 96-well tissue culture plates in the presence of fullerene peptides in PBS buffer with a final volume of 100  $\mu$ L. Cells were grown for 48 h at 37 °C in a CO<sub>2</sub> incubator. Relative cell growth was determined by Cell Counting Kit-8 (CCK-8) cell proliferation assay as described by the manufacturer using an automated ELISA plate reader.

**Reference**

- <sup>1</sup> H. W. Kroto, J. R. Heath, S. C. O'Brien, R. F. Curl and R. E. Smalley, *Nature*, 1985, **318**, 162.
- <sup>2</sup> W. Kratschmer, L. D. Lamb, K. Fostiropoulos, and D. R. Huffman, *Nature*, 1990, **347**, 354.
- <sup>3</sup> Z. Markovic and V. Trajkovic, *Biomaterials* 29 (2008) 3561.
- <sup>4</sup> R. Partha and J. Conyers, *Nanomedicine*, 2009, **4**, 261.
- <sup>5</sup> S. Durdagi, T. Mavromoustakos, N. Chronakis, and M. G. Papadopoulos, *Bioorg. Med. Chem.*, 2008, **16**, 9957.
- <sup>6</sup> S. H. Friedman, D. L DeCamp, R. P. Sijbesma, G. Srdanov, F. Wudl, and G. L. Kenyon, *J. Am. Chem. Soc.*, 1993, **115**, 6506.
- <sup>7</sup> A. Hirsch, *AIP Conference Proceedings*, 2005, **86**,581.
- <sup>8</sup> J. Yang, L. B. Alemany, J. Driver, J. D. Hartgerink, and A. R. Barron, *Chem.Eur. J.*, 2007, **13**, 2530.
- <sup>9</sup> E. Nakamura, H. Tokuyama, S. Yamago, T. Shiraki, and Y. Sugiura, *Chem. Soc. Jpn.*, 1996, **69**, 2143.
- <sup>10</sup> C. Supuran, *Nat. Rev. Drug Discovery.*, 2008,**7**, 168.
- <sup>11</sup> M. Ferrari, *Nat. Rev. Cancer*, 2005, **5**, 161.
- <sup>12</sup> R. Partha and J. Conyers, *Nanomedicine*, 2009, **4**, 261.
- <sup>13</sup> J. Yang, K. Wang, J. Driver, J. Yang, and A. R. Barron, *Org. Biomol. Chem.*, 2007, **5**,260.
- <sup>14</sup> J. Kang,P.G Rychahou,T. A. Ishola, J. M. Mourot, B. M. Evers, and D. H. Chung, *Oncogene*, 2008, **27**, 3999.
- <sup>15</sup> J. Kang, P. G. Rychahou, T. A. Ishola, J. Qiao, B. M. Evers, and D. H. Chung, *Biochem. Biophys. Res. Commun.*, 2006, **351**, 192.



- <sup>16</sup> A. Maresca, C. Temperini, H. Vu, N. B. Pham, S. A. Poulsen, A. Scozzafava, R.J. Quinn, and C. T. Supuran, *J. Am. Chem. Soc.*, 2009, **131**, 3057; (b) A. Maresca, C. Temperini, L. Pochet, B. Masereel, A. Scozzafava, A.; and C. T. Supuran, *J. Med. Chem.*, 2010, **53**, 335.
- <sup>17</sup> K. A. Spriggs, L. C. Cobbold, C. L. Jopling, R. E. Cooper, L. A. Wilson, M. Stoneley, Mark; M. J. Coldwell, Poncet, S. Didier; M. Ya-Ching; and J. Simon; M. Bushell, and A. E. Willis, *Mol. Cell. Biol.*, 2009, **29**, 1565.
- <sup>18</sup> L. J. Draeger and G. P. Mullen, *J. B. Chem.*, 1994, **269**, 1786.
- <sup>19</sup> S. Durdagi, C. T. Supuran, T. A. Strom, N. Doostdar, M. A. Kumar, A. R. Barron, T. Mavromoustakos, and M. G. Papadopoulos, *J. Chem. Info. Model.*, 2009, **49**, 1139.
- <sup>20</sup> A. Innocenti, S. Durdagi, N. Doostdar, T. A. Strom, A. R. Barron, and C. T. Supuran, *Bioorg. Med. Chem.*, 2010, **18**, 2822.

## Appendix A

### Publications

1. Nanoscale enzyme inhibitors: Fullerenes inhibit carbonic anhydrase by occluding the active site entrance . A. Innocenti, S. Durdagi, N. Doostdar, T. A. Strom, A. R. Barron, and C. T. Supuran, *Bioorg. Med. Chem.*, 2010, **18**, 2822.
2. In silico drug screening approach for the design of magic bullets: a successful example with anti-HIV fullerene derivatized amino acids. S. Durdagi, C. T. Supuran, T. A. Strom, N. Doostdar, M. A. Kumar, A. R. Barron, T. Mavromoustakos, and M. G. Papadopoulos, *J. Chem. Info. Model.*, 2009, **49**, 1139.
3. The role of silicon containing compounds in the formation and morphology of calcific band keratopathy precipitates. N. Doostdar, C. J. Manrique, M. B. Hamill, and A. R. Barron, 2010, submitted for publication.
4. Synthesis of calcium-silica composites: a route towards an *in-vitro* model system for calcific band keratopathy precipitates. N. Doostdar, C. J. Manrique, M. B. Hamill, and A. R. Barron, 2010, submitted for publication.
5. New therapeutic agents for treatment of calcific band keratopathy precipitates. N. Doostdar, C. J. Manrique, M. B. Hamill, and A. R. Barron, 2010, in preparation.